THE EFFECTS OF NI NANOPARTICLE ADDITIVES ON THERMODYNAMIC EVENTS IN COMMERCIAL NI BASED BRAZE ALLOY

by

Cody LeSage

A Thesis Submitted in

Partial Fulfillment of the

Requirements for the Degree of

Master of Science

in Engineering

at

The University of Wisconsin-Milwaukee

May 2024

ABSTRACT

THE EFFECTS OF NI NANOPARTICLE ADDITIVES ON THERMODYNAMIC EVENTS IN COMMERCIAL NI BASED BRAZE ALLOY

by

Cody LeSage

The University of Wisconsin-Milwaukee, 2024
Under the Supervision of Professor Dr. Benjamin Church

The use of nanomaterials in brazing applications has become more prevalent with the increasing understanding of the underlying thermodynamic events during the brazing process. Their influence on an already modified system, via melting point depressants, is not well understood. In this investigation, the influence of both nanoparticle size and weight percent of nanoparticle additive are studied to determine the relationship on thermodynamic events. Differential scanning calorimetry was used to measure the energy flow throughout the system during the brazing events. Scanning electron microscopy was used qualitatively to view the resulting brazed region. The results indicate a direct relationship between nanoparticle additive size and weight percent and the resulting melting and solidification temperatures. The resulting enthalpy of the braze event also decreased in magnitude with the increase in weight percent of nanoparticle additive. Understanding the thermodynamic effects of nanoparticle additives on commercial alloys containing melting point depressants can lead to a “best of both worlds” scenario.

To

My Exceptional Wife

My Loving Family

Every Coach, Mentor, Teacher, and Friend

To All Whom Have Supported Me and Guided Me

TABLE OF CONTENTS

LIST OF FIGURES

LIST OF TABLES

1. Introduction

Nanotechnology has revolutionized many industries through the application and understanding of the properties of nanomaterials to best fit their respective niches. Processes that have been utilized throughout much of recorded human history, such as brazing, are no exception. Brazing is a process in which two materials are joined together by melting and flowing a filler or braze metal in the joint with the braze metal having a lower melting point than either of the base materials. This liquid-solid bonding process is differentiated from welding in which similar base materials are melted. The complimentary addition of a nanomaterial into an existing braze alloy prior to brazing can lead to significantly different effects. These can include but are not limited to enhanced joint strength and braze alloy diffusion [1].

A significant amount of research has been conducted on the effect nanoparticles (NP) have on the more conventional characteristics or outputs of the brazing process, including: joint strength [2], wettability [3], and melting point depression [4] [5] among others. For example, Sharma et al. [3] showed the wettability or spread ratio of an Al-12Si-20Cu braze filler could be increased by the addition of La_2O_3, SiC, or ZrO_2 nanoparticles. See Figure 1 for their results. Less, though not uncommon, research has been conducted on the underlying kinetics and thermodynamics of the brazing process when nanoparticles are included. In one example, it was shown by Akhtar et al. [6]that the addition of Al_2O_3 nanoparticles to an electrodeposited Cu coating accelerated and altered the bonding process. Figure 2 shows the resulting shear strengths of the modified and unmodified Cu interlayer with respect to time. An opposite relationship was seen. The shear strength of the Al_2O_3 nanoparticle modified Cu interlayer was inversely proportional to time whereas the unmodified Cu interlayer showed a directly proportional relationship. The

Al_2O_3-Cu mechanism of bonding was described as more characteristic of brazing by which the eutectic liquid wets the surfaces and spreads by capillary action. The pure Cu mechanism was defined by a smaller volume of eutectic liquid, leading to the bond strength developing through the continued interdiffusion between the interlayer and base metals. Also, the eventual formation of copper-aluminides further strengthens the bond. This shows that an understanding of the flow of energy and matter within the system could lead to specific and lean applications in the future.

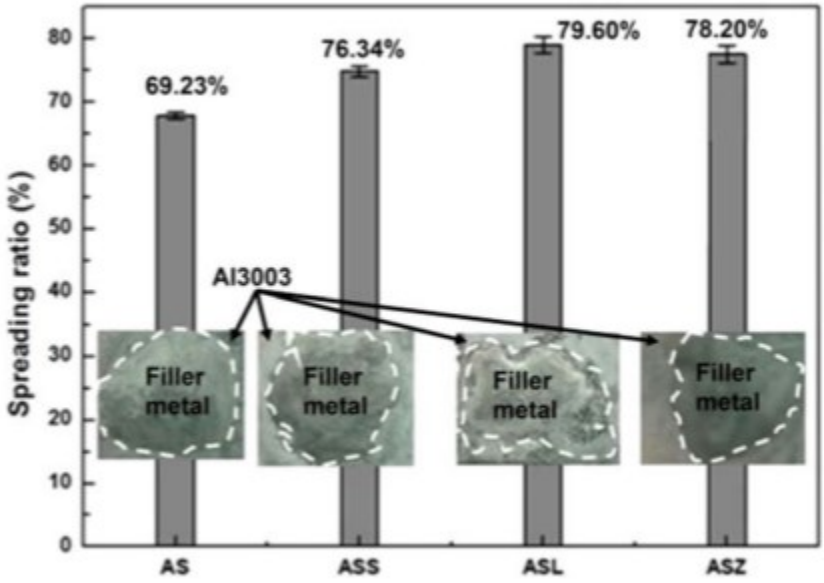

Figure 1 - Spreading ratio of Al-Si-Cu alloy modified with varying nanomaterials. AS: The Al-12Si-20Cu braze alloy matrix. ASS: Alloy matrix with SiC nano-additive. ASL: Alloy matrix with La_2O_3 nano-additive. ASZ: Alloy matrix with ZrO_2 nano-additive. [3]

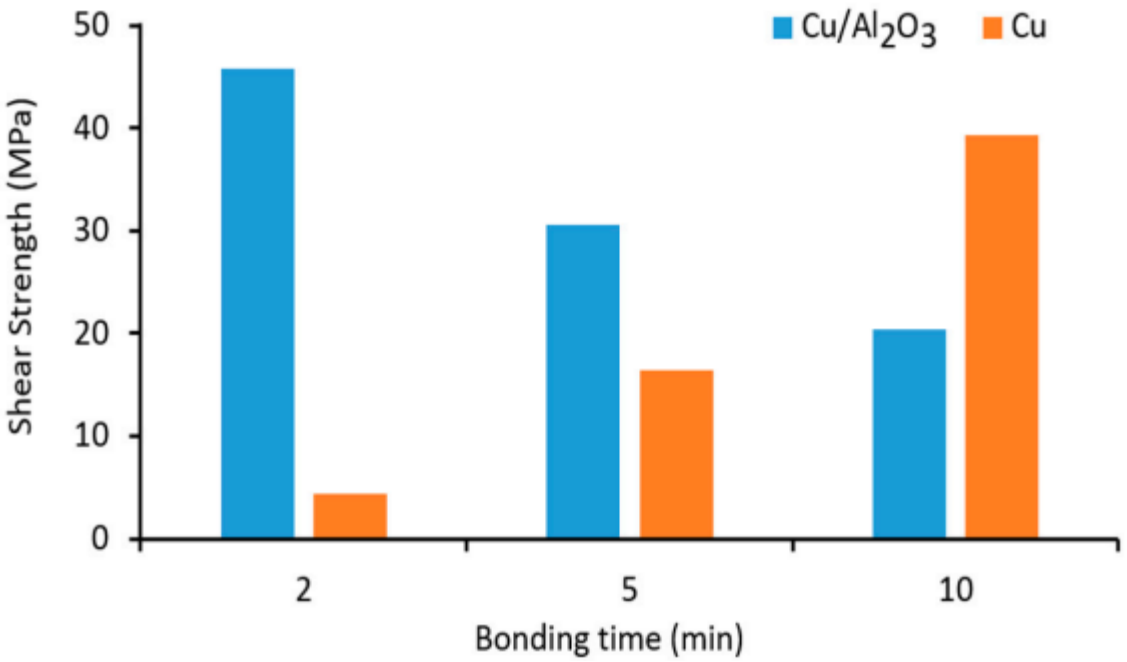

Figure 2 - Shear strength as a function of bond time with Al2O3 nanoparticle modified Cu interlayer and pure Cu interlayer. [6]

In this investigation, the use of differential scanning calorimetry (DSC) is applied to measure the flow of energy and changes of state within a system consisting of a single puck of 316L stainless steel, a nickel based Hoganas braze alloy discussed later, and nickel nanoparticles. This system was chosen due to the prevalent use of 316L stainless steel and the commercial availability of the Hoganas nickel based braze alloy.

1.1 Goal

The purpose of this investigation was to evaluate the effect of particle size and quantity of nanoparticles in a braze alloy on diffusion and melting characteristics. With earlier diffusion into the base material, safer practices could be utilized in brazing processes leading to potentially more robust brazing techniques. There exists a gap in the publicly available knowledge on the thermodynamic evolution of commercial braze systems containing nanoparticle additives. These already have sufficient complexity but looking at the system holistically may lead to novel

approaches. One potential example, a commercial product line could exist of nano-material additives for modifying braze alloys. With some guidelines for chemical compatibility and homogenization techniques an end user could modify their existing braze alloy to meet their specific needs. In a similar example, with sufficient equipment a company could custom create braze alloys for their customers based on joint requirements provided. With a broader holistic thermodynamic understanding it could be possible to determine the required material and environmental inputs based on the desired outputs within a constrained system.

1.2 Scope

This investigation is concerned with a simplified look into a system containing a single puck of 316L stainless steel, Hoganas Brazelet® Ni613 braze alloy, and Ni nanoparticles. The actual system of brazing is significantly complex with many variables which are not covered and knowingly omitted. These omissions include pressure [7], surface cleanliness [8], temperature [2], braze period [9], base material porosity [9], wettability [10], surface tension [10], grain boundary diffusion [11] [12], and joint clearance [13].

1.3 Background

316L (SS) is a popular steel alloy used in industries ranging from automotive, manufacturing, aerospace, and construction among others. Composition of 316L SS can be found in Table 10 of the APPENDIX. Some of the desired characteristics of 316L SS is its low carbon content, resistance to weld decay, corrosion resistance, and it ability to withstand higher temperatures than 316 SS. According to the International Stainless Steel Forum, in 2019 global stainless steel meltshop production reached over 52.2 million metric tonnes. [14]

BrazeLet® Ni613 is a nickel-based filler powder developed by Hoganas for high temperature brazing. It was specifically designed for exhaust gas recirculation coolers commonly found in internal combustion engines. The recommended brazing temperature for BrazeLet® Ni613 is 1080°C and the filler material exhibits excellent corrosion resistance.

The generally accepted process steps for brazing can be found in Figure 3. Step 1 involves understanding and designing the joint. Selecting the filler alloy based on the capabilities and limitations of the material is key. Surface preperation, step 2, involves removing dirt, debris, and other surface effects that may inhibit the bond. In step 3, surface oxides are removed generally by the application of a flux. The flux also prevents the formation of oxides while the metal is heated. Flux may not be needed if the brazing operations are conducted under an inert or reducing atmosphere, such as during vacuum brazing. In step 4 the filler material is added and heated to above its melting temperature. Brazing differs from soldering in that the melting temperature of the braze material is generally above 450°C. The filler material then wets the surfaces and flows into the joint via capillary action. During step 4 is when the liquid filler diffuses into the base material. During step 5, the filler cools and the subtrates are bonded together.

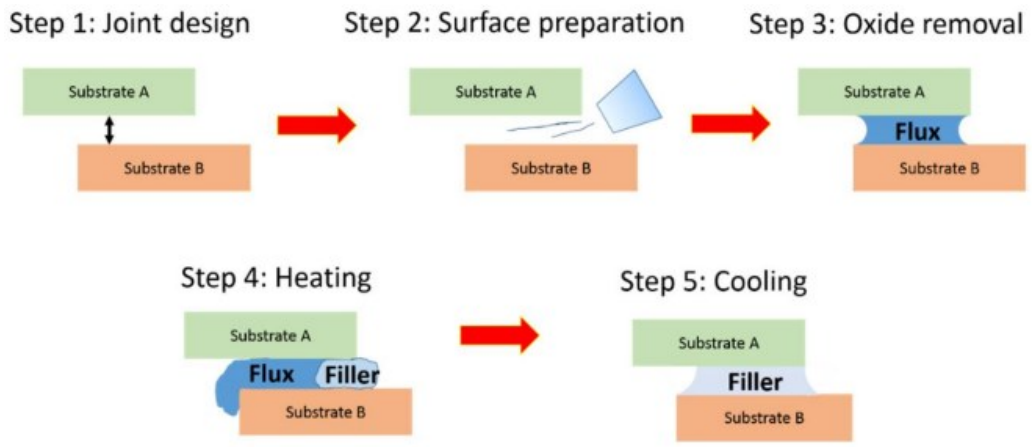

Figure 3 - Generalized process steps for brazing. [10]

1.4 Literature Review

Much work has been completed in the 21st century on brazing dissimilar materials, particularly in unique cases utilizing novel materials. Ceramic brazing, though difficult and complex, can be completed. The use of Ag-Cu-Ti has been proven as a successful filler material [15] as well as a novel $50Bi_2O_3$-$40B_2O_3$-10ZnO glass braze for sapphire/sapphire joints [16]. Bulk metallic glass, though having impressive mechanical and corrosion resistant properties [17], tends to crystallize during joining techniques, such as brazing, removing the desired characterics of the material. Kim et al. [18] have shown that with an active metal Zn-Ag-Al filler a joint between Cu-Ni-Zr-Ti bulk metal glass and steel is possible. [18]

Another area that has seen much attention is the use of nanomaterials in brazing, either with nanomodified fillers or solely nanomaterial fillers; both via loose particles and nanostructures. Bridges et al. utilized Ni nanowires (NW) and NPs to braze a lap joint of Inconel 718 with a bond strength of over 300 MPa [11]. They found that a faster heating rate, higher maximum bonding temperature, and a larger particle size resulted in a higher bond strength [19]. Eluri et al. [20] created a hermetic joint in 316L stainless steel substrates utilizing ~9 nm Ni nanoparticles under

2 MPa of pressure during brazing. [20] This joint, shown in Figure 4, was able to withstand up to the tested pressure of 70 psi. Lehmert et al. demonstrated an ability to apply nanostructures as a novel low-temperature filler material for brazing applictions. [21] As shown in Figure 5, a Cu/AlN nano-multilayer was depositied via magnetron sputtering with 200 repetitions of 10 nm thick AlN and 10 nm thick Cu.

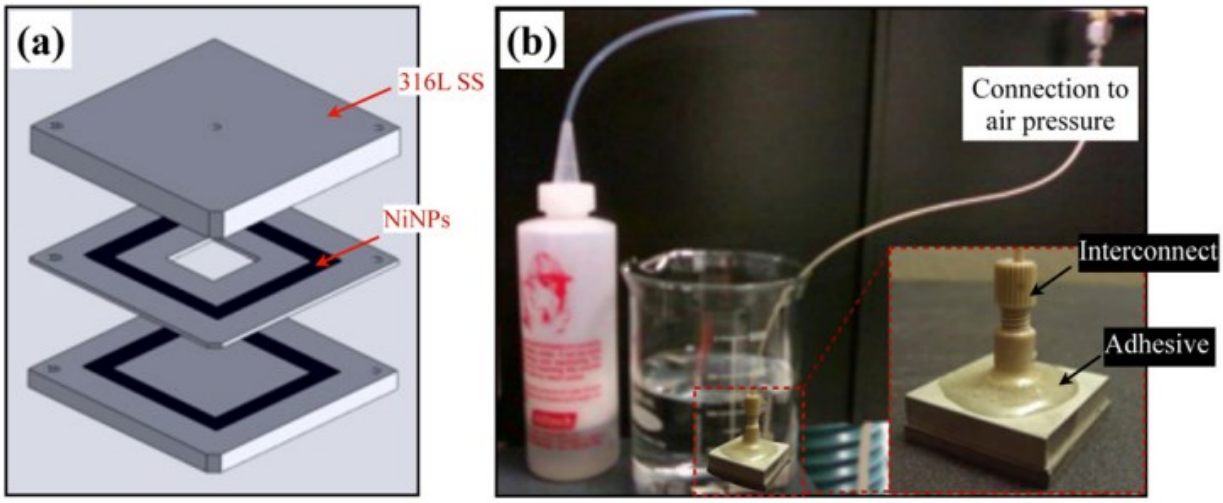

Figure 4 - (a) test article used for evaluating Ni NP-assisted diffusion brazing; and the (b) setup used for leak testing. [20]

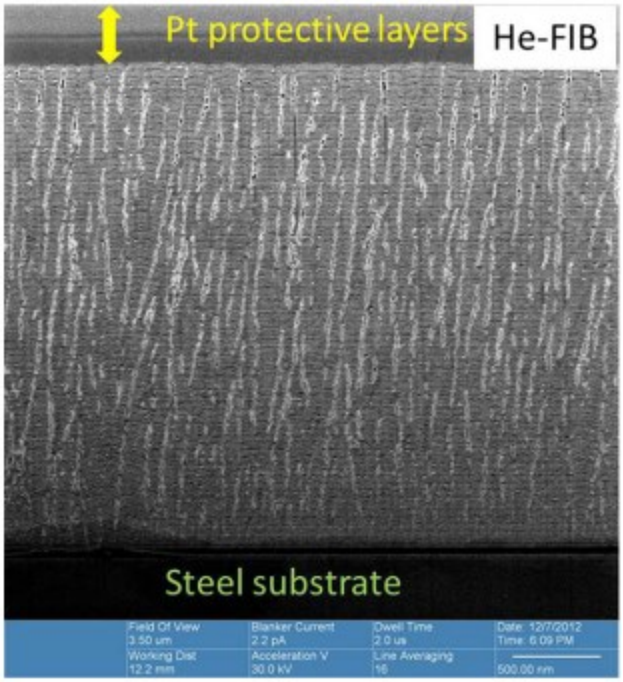

Figure 5 - Cross-sectional electron micrograph of Cu/AlN nano-multilayer coatings on a steel substrate after 200x repetitions. [22]

Jeevanandam et al. [23] thoroughly reviewed nanomaterials sources and toxicity. While nanomaterials are necessary for many aspects of biological processes, others carry with them an inherent danger and toxicity to humans and other life. This toxicity can be due to many different factors: dose and exposure, aggregation and concentration, particle size, particle shape, surface area, crystal structure, surface functionalization, and pre-exposure. [23] Yet, these same factors are what give nanomaterials and nanostructures their unique desirable characteristics. As important as it is to create novel nanomaterials, it is equally important to be able to handle these materials safely. As such, nanoparticles are commonly suspended in an organic paste [24] [25] or other type of solution.

One common use for nanomaterials in braze alloys takes advantage of the lower melting point of nanoparticles compared to the bulk material. The melting point of 50 nm copper

nanoparticles has been shown to be lowered to 633°C [5] which is much lower than the bulk melting temperature of 1084°C. It has also been demonstrated and modeled for vanadium in which the melting point is inversly proportional to the nanoparticle size [26] as shown in Equation 1. Where T_{mb} is the melting temperature of the bulk, *d* is the particle diameter, and β = 0.944. This agrees with the well studied and understood Gibbs-Thomson effect as shown in Equation 2 which refers to the observation that smaller crystals have a lower melting temperature than larger crystals. Where σ_{sl} is the solid-liquid interface energy per unit area, H_f is the bullk enthalpy of fusion per gram, ρ_s is the density of the solid, and *r* is the radius of the nanoparticle. This is because there is a more positive interfactial energy required to form smaller particles, due to the higher curvature, exhibiting an increased vapor pressure.

$$T_m = T_{mb}(1 - \frac{\beta}{d})$$

Equation 1

$$\Delta T_m(x) = T_{mb}\frac{3\sigma_{sl}}{H_f \rho_s r}$$

Equation 2

This fundamental lower melting point characteristic of nanoparticles was theorized as early as 1909 [27] [28] and first captured via an electron microscope in the 1960s and 1970. [29] Boron and silicon have long been traditionally used as melting point depressants for braze alloys but it is well documented that these additional elements form undesirable intermetallic phases [30] [31] [32], borides and silicides which compromise the integrity of the joint. Ghasemi et al. [33]

succinctly detail this point. Figure 6 outlines a general structure for three different microstructure zones in a Ni-based alloy with a boron-containing filler metal: the isothermal solidification zone (ISZ), the athermal solidification zone (ASZ), and the diffusion-affected zone (DAZ). [33] The ISZ region contains little to no boron but rather a solid solution phase. The driving force for this region is induced compositional changes by interdiffusion of the base metal and the filler metal at a constant temperature. The ASZ forms during the cooling of the residual liquid via a eutectic solidification reaction. These products consist of many hard and brittle boride containing intermetallic compounds. The DAZ is primarily influenced by the diffusion of boron into the base metal which leads to the precipitation of borides in the substrate region. Figure 6 shows the average microhardness values of the various regions discussed. As the ASZ contains the largest amount of boron-containing intermetallics it confirms that it would have the highest average hardness of all boron-containing measured regions. These hard and brittle boron-intermetallics degrade the mechanical strength of the braze joint.

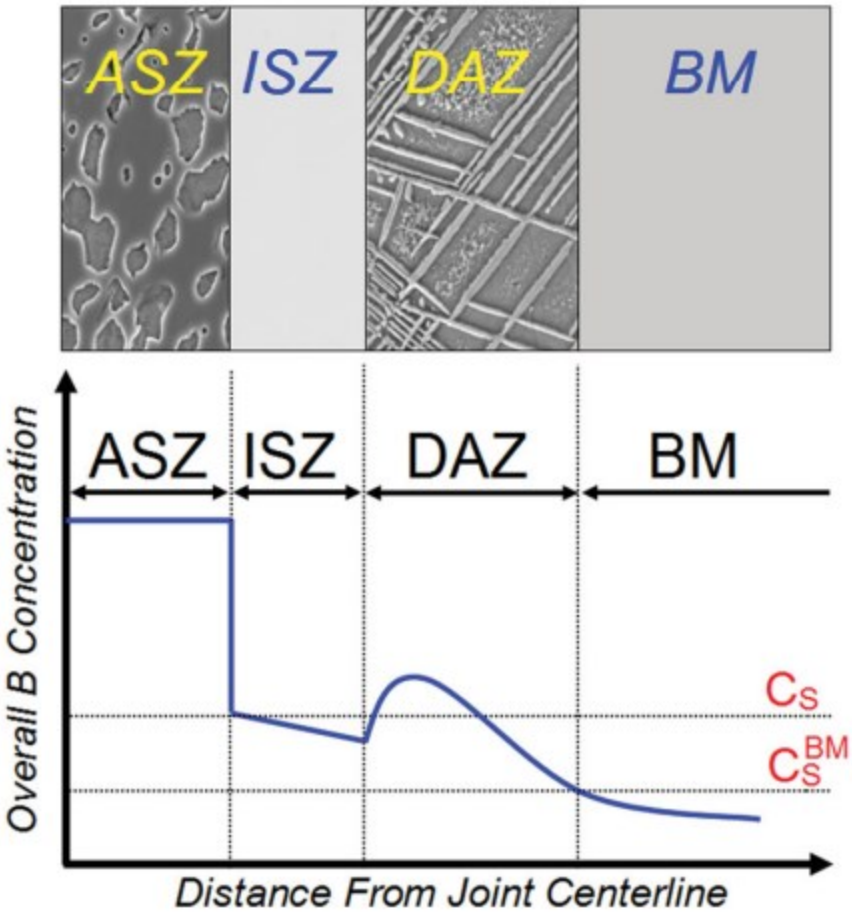

Figure 6 - Schematic microstructure of a typical Ni-based alloy with estimated boron concentration gradient across the bond region. C_S is boron solubility at the solid/liquid interface. C_S^{BM} is the boron solubility in the base metal. [34]

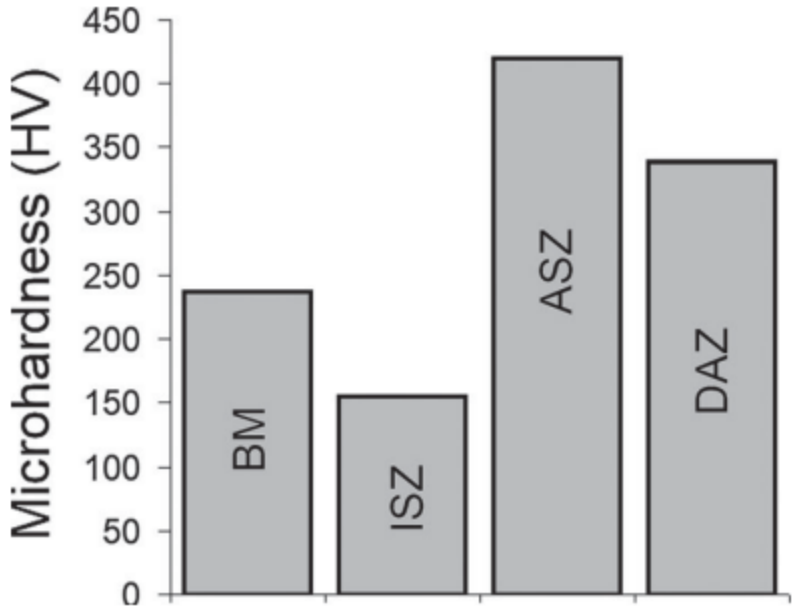

Figure 7 - Measured average hardness values of various microstructure regions obtained by Ghasemi et al. [33]

A lot of research has been thoroughly completed to remove the dependance on these melting point depressents. Such work including the use of nanoparticles [35] and high entropy alloys [36] [37] have reduced the number of possible brittle phases. Tiwari et al. [38]demonstrated a roughly 25% higher shear strength bond with Ni NP-assisted diffusion brazing than conventional nickel phosphorus diffusion brazing or diffusion bonding. [38] This was reportedly due to less void fraction and better diffusion penetration without brittle secondary phases along the bond line.

The effects of particle size on thermodynamic events such as melting, solidification, and phase changes has been thoroughly researched [39] [40] [41] [42] [43] [44] [6]. It can be generally stated that as particle size decreases in a binary eutectic system, there will be a reduction in the eutectic temperature, constituent melting temperature, and a lowering of the liquidus and

solidus boundaries. There will also be a shift in the eutectic composition. Kumar et al. [44] shows this in Figure 8 for an Al-Si binary system. These changes are generally attributed to a larger surface-to-volume ratio and excess Gibbs energy. Though much work has been done on simple, ideal, or theoretical systems, not as much work has been completed on modifying existing commercially available braze materials.

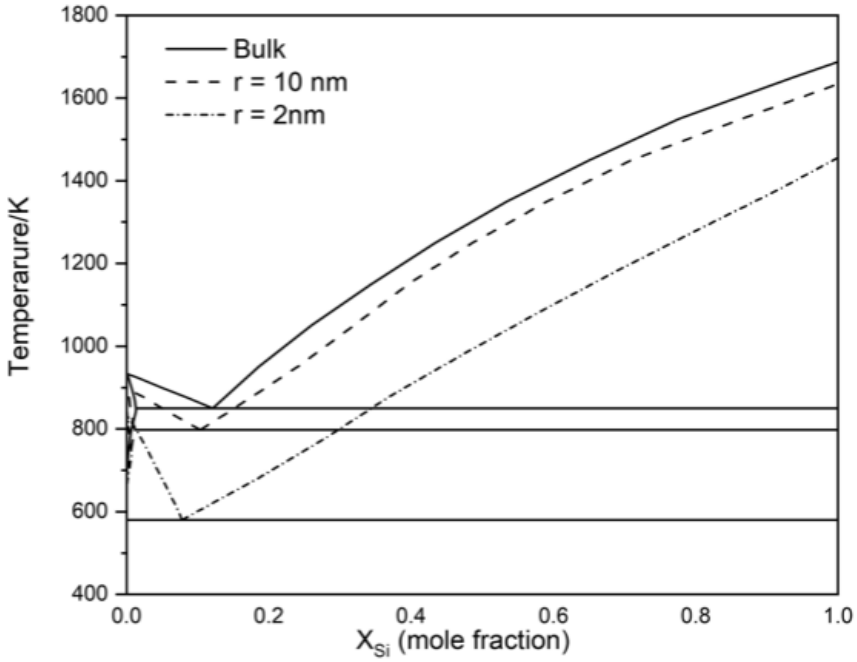

Figure 8 - Calculated phase diagram of Al-Si nanoparticles of varying particles size. [44]

DSC is a common tool for studying the thermal evolution of nanoparticles in braze alloys. This technique is commonly used to determine or verify melting temperature of the nanomaterials in question; [45, 46, 3, 8, 5, 40] commonly comparing experiment to theoretical calculations. DSC can also be used to study other phenomenon. Eluri et al. [47]experimentally showed that 5 nm Ag NPs exhibit a phase change below the eutectic temperature of an Al-Ag system but 50 nm NP do not. Seen in Figure 9 [47], the 5 nm Ag NPs show a phase change beginning around 430°C and ending near 567°C. This phenomenon generally occurs where the eutectic

melts first and then slowly reaches the liquidus temperature before melting completely. As shown, this does not happen with the 50 nm Ag NPs.

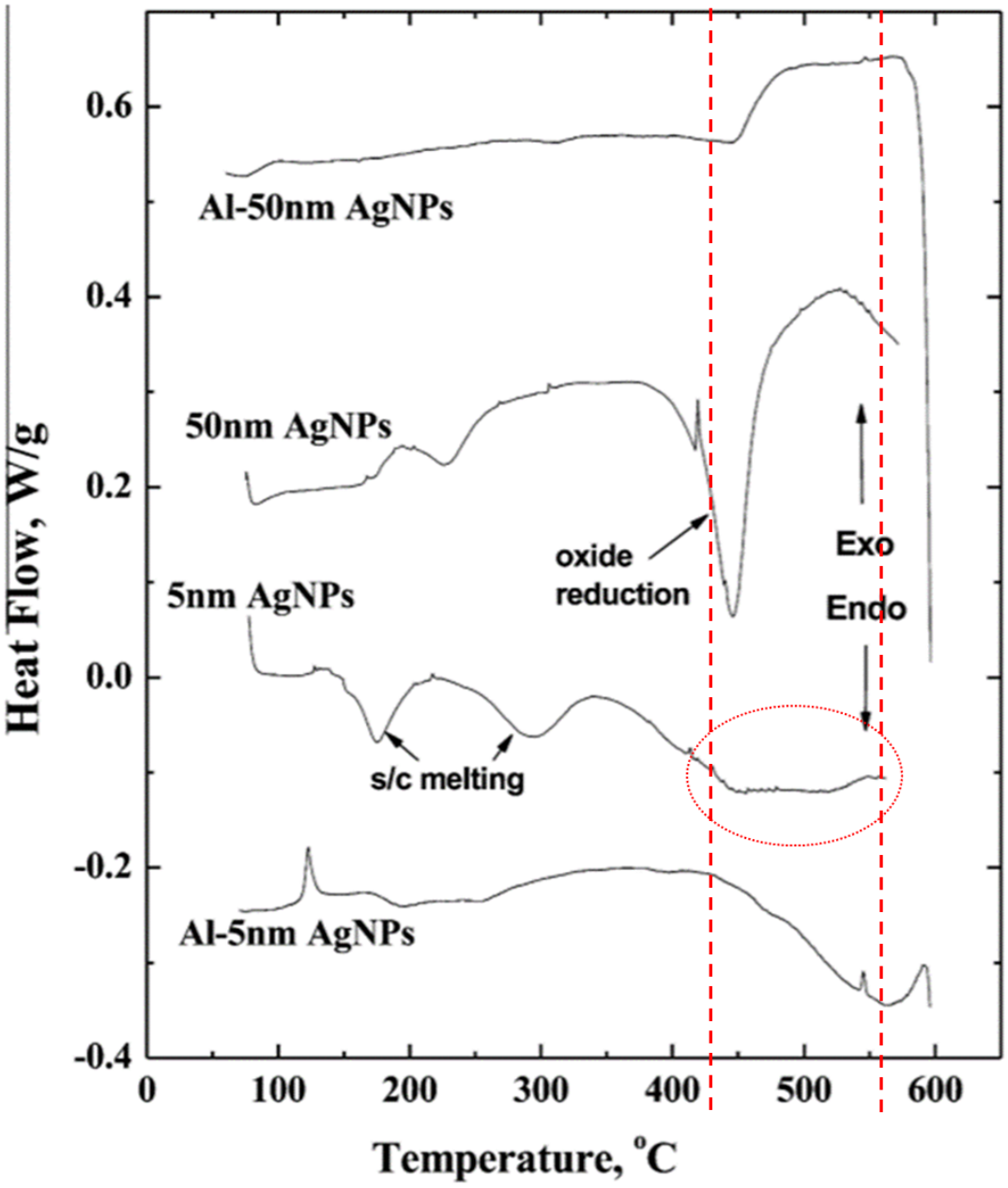

Figure 9 - -DSC thermal profile of Ag NPs and Al coated with Ag NPs at a heat rate of 25°C/min [47]. Vertical dotted lines representing approximately 430°C and 567°C. Red dotted circle showing a phase change seen in the 5nm Ag NPs but not in the 50nm Ag NPs.

2. Experimental Procedure

2.1 Preparation of Base Metal

Base metal samples were prepared from a 5 mm diameter rod of 316L stainless steel cut with a diamond saw into roughly 2 mm thick pucks. These pucks were then mounted in Bakelite and polished down to a 1 micron alumina suspension finish. The pucks were then removed from the Bakelite and cleaned before use. This process yielded a polished face of the puck that was relatively flat and did not have any significant rounding of the edges.

2.2 Preparation of Filler Metal

The base braze alloy used was Hoganas BrazeLet Ni613 with a nominal particle size less than 106µm. Four filler metal batches were then created with 5 wt% nickel nanoparticles purchased from US Research Nanomaterials of the following sizes with 3N purity: 20 nm, 40 nm, 70 nm, and 800 nm. The composition and impurities for both the base alloy and the nanoparticles can be found in the APPENDIX. Each batch was then homogenized via a vortex mixer for 5 minutes.

Utilizing the same base material and nickel nanoparticle supply, two more samples were prepared under similar conditions. Hoganas Brazelet Ni613 with 20 wt% 40 nm Ni nanoparticles and 40 wt% 40 nm Ni nanoparticles. Each was also homogenized via a vortex mixer for 5 minutes.

The Hoganas Brazelet Ni613 braze alloy was selected due to its availability and Ni-based composition. NPs were purchased from US Research Nanomaterials due to cost, availability of pure Ni NPs, the ability to find a single source for all NP additives, and range of NP sizes offered. Nanoparticles sizes were selected to be able to see results across a wide range.

2.3 Brazing and Measurement Setup

A Netzsch STA 449-F1 was used both for brazing procedures and differential scanning calorimetry measurements. 50 mg of braze alloy mixture was placed into an alumina crucible with one puck of the 316L stainless steel metal with the polished surface in contact with the filler material. The crucible lid was then put in place and the sample system was loaded into the Netzsch. An identical empty alumina crucible was used for the reference. The chamber was sealed and then vacuum purged and flushed with argon two times prior to the start of a test. A schematic of the sample setup can be seen in Figure 11.

Each braze alloy was measured by DSC in triplicate utilizing the following procedure. All 5 wt% samples were measured under 25 mL/min of argon gas while the 20 wt% and 40% samples were measured under 15 mL/min argon gas and 10 mL/min of a 95% argon and 5% hydrogen. This was done to remove any surface bound oxygen from the nanoparticles within the blend. The Ar-H blend was tested and shown to not affect the outcome of DSC measurements. The temperature schedule for each sample followed the profile in Figure 10 and was as follows:

1. Ramp from ambient temperature to 1200°C at 10°C /min
2. Hold at 1200°C for 5 minutes.
3. Cool to 400°C at 10°C /min.

The system was then allowed to cool back to ambient temperature without protective gas as data collection stopped.

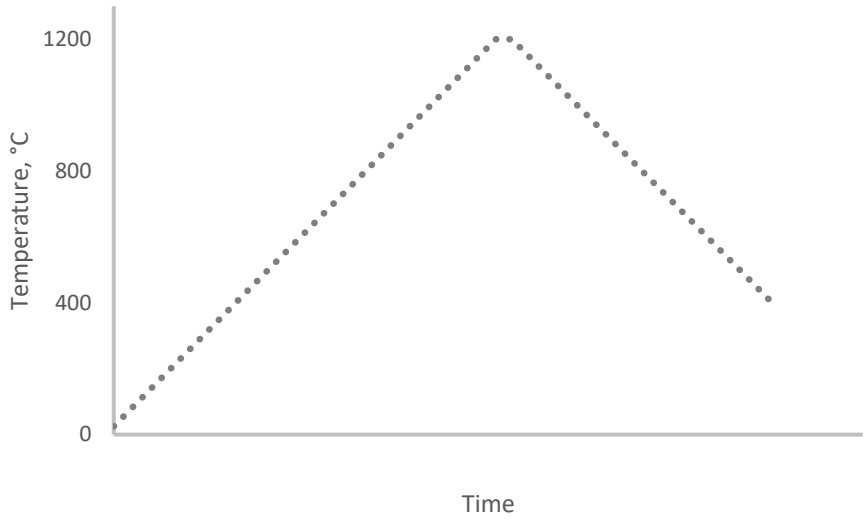

Figure 10 - DSC program used for all samples.

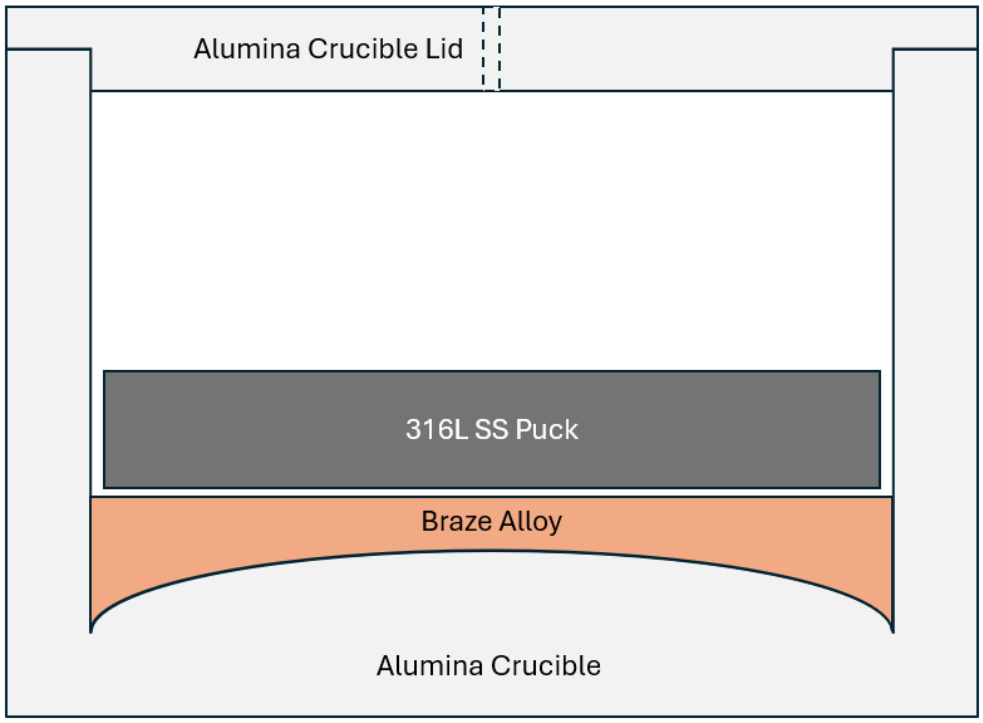

Figure 11 - Schematic setup of crucible, 316L SS puck, and braze alloy.

3. Results and Analysis

The Netzsch Proteus Thermal Analysis software was used to study the resulting data from the DSC measurements. This software was used to determine the onset temperature, peak

temperature, and enthalpy for each experimental run. Enthalpy is determined by integrating the area of the event peak and the interpolated baseline between the beginning and end of the event. Each series of runs were compared against an unmodified “baseline” of the Hoganas Brazelet Ni613 which contained no added Ni NPs. A representative DSC scan of the baseline samples can be seen in Figure 12 with Figure 13 and Figure 14 detailing heating and cooling events of interest, respectively. Further results of this investigation will focus on these events of interest. The solidus and liquidus peaks for both melting and solidification overlap due to the primary Ni-Cr Hoganas alloy composition having a very narrow alpha-liquid region. This can be seen in the Ni-Cr phase diagram in Figure 15. Peaks were identified using the Netzch Proteus Thermal Analysis software.

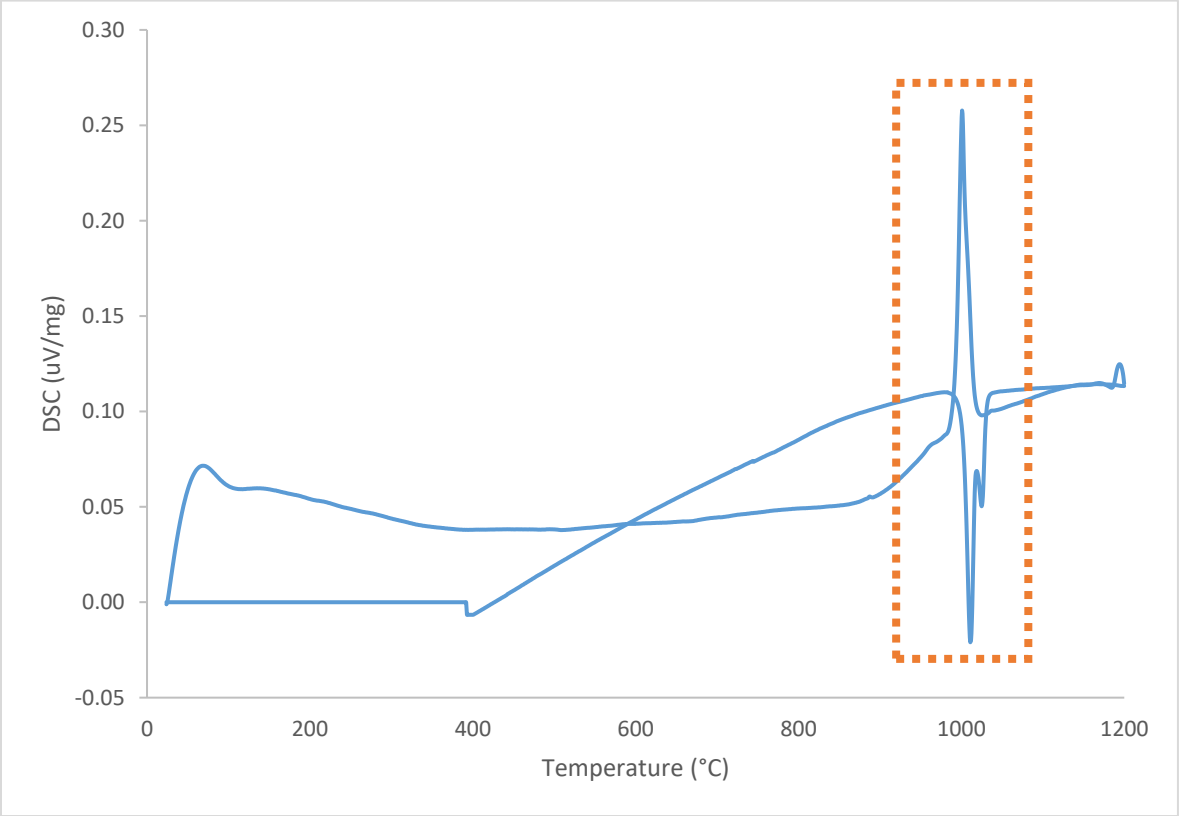

Figure 12 – Representative DSC scan of baseline alloy. Region of interest containing melting and solidification events called out in dotted box.

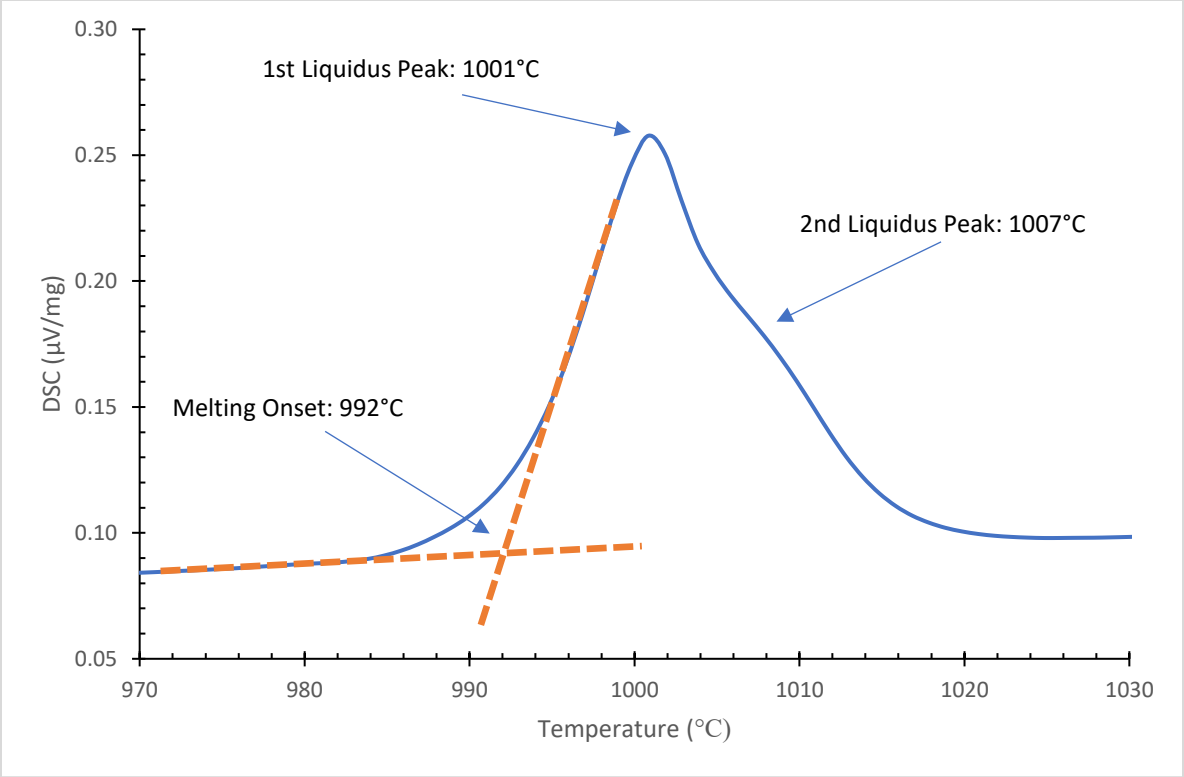

Figure 13 – Baseline DSC results for heating events.

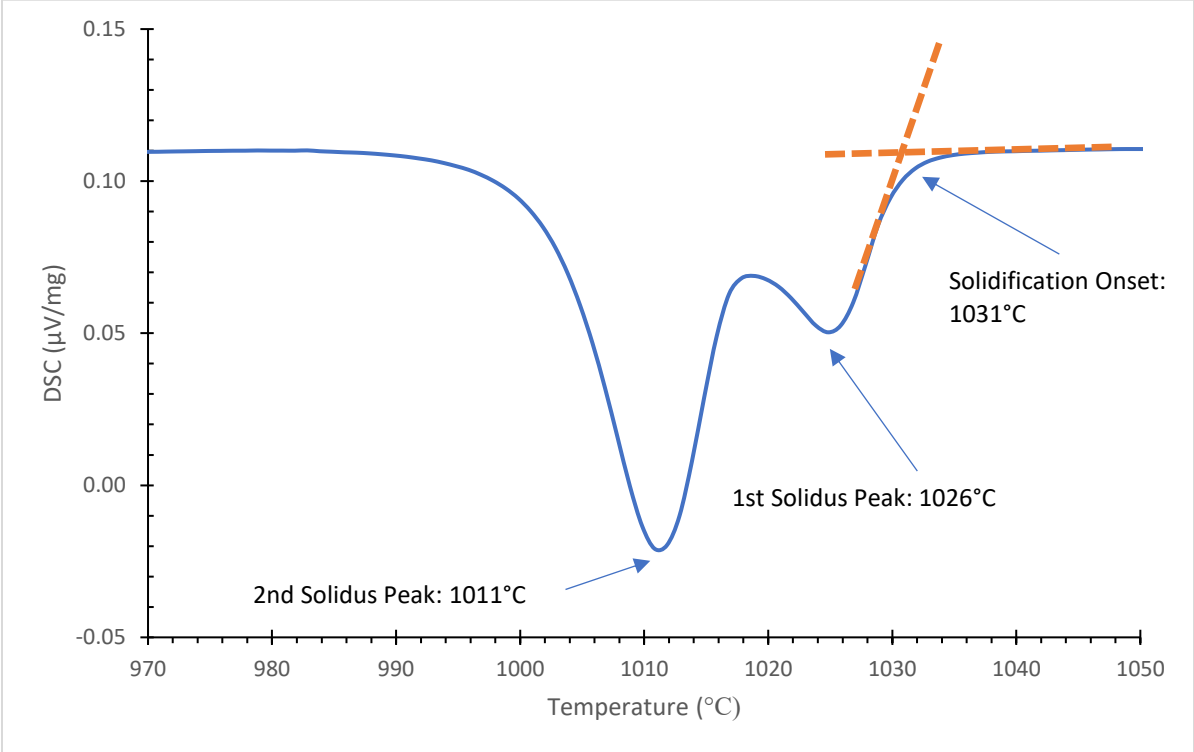

Figure 14 - Baseline DSC results for cooling events.

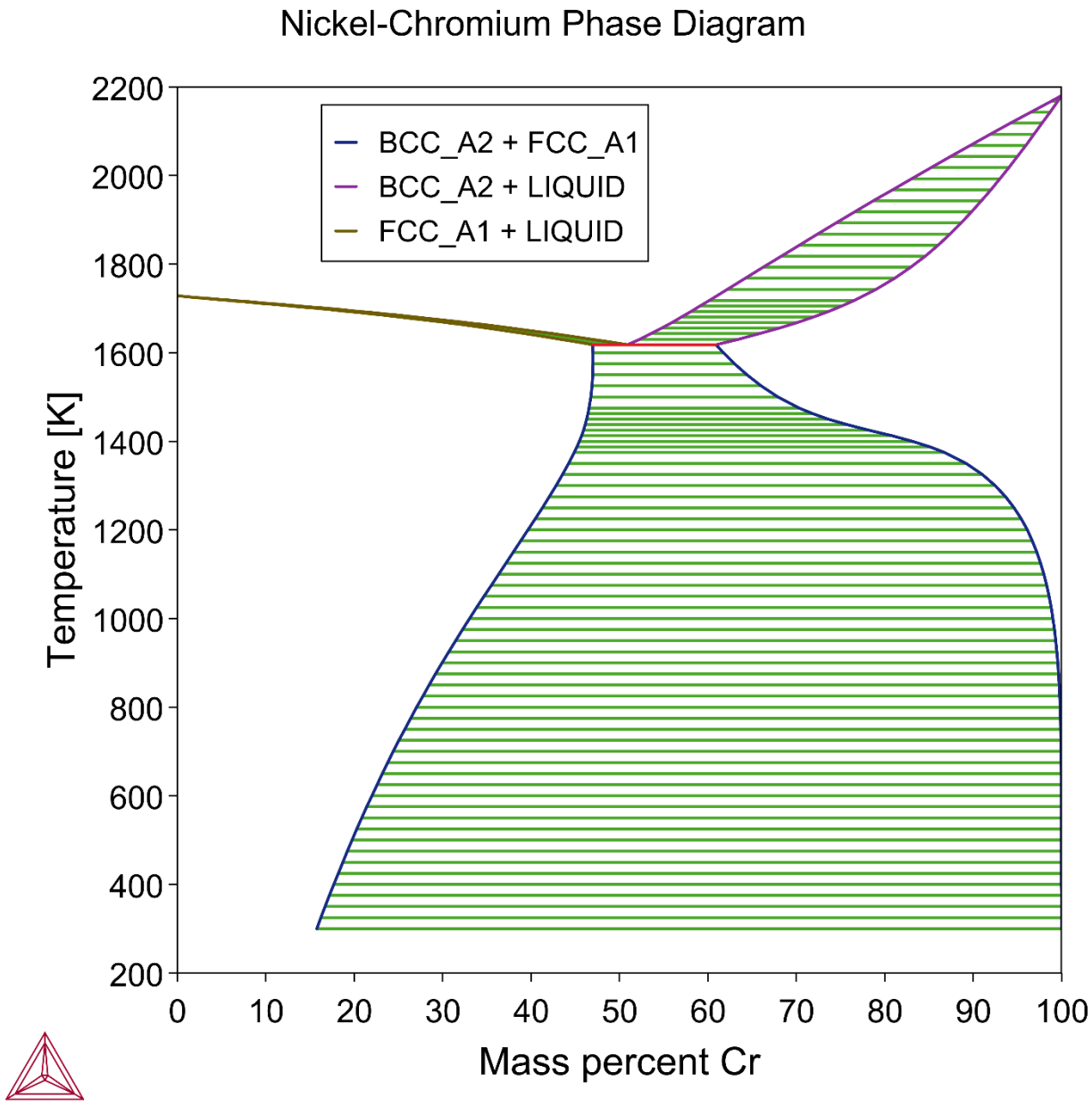

Figure 15 - Ni-Cr phase diagram generated by Thermocalc.

3.1 Influence of increasing Ni additive particle size

The DSC results for the first series of runs, 5 wt% Ni nanoparticle modified braze alloy of sizes 20 nm, 40 nm, 70 nm, and 800 nm, are shown in Figure 16. As can be seen, each run is similar in shape and size with onset temperatures and peak temperatures being similar and the entire melting event overlapping. Figure 17 shows the solidification event for the same samples. The 800nm 5 wt% and the 70 nm 5 wt% samples both show a bimodal distribution similar to the

baseline results. The 40 nm 5 wt% and the 20 nm 5 wt% samples do not show clear distinct bimodal peaks but rather a single peak. This demonstrates the α + L region narrowing. The higher temperature peak, the liquidus, shifts to a lower temperature, while the lower temperature peak, the solidus, remains the same. Numerical results for the 5 wt% samples can be found in Table 1 and Table 2. Table 3 shows the difference in these values from the baseline results.

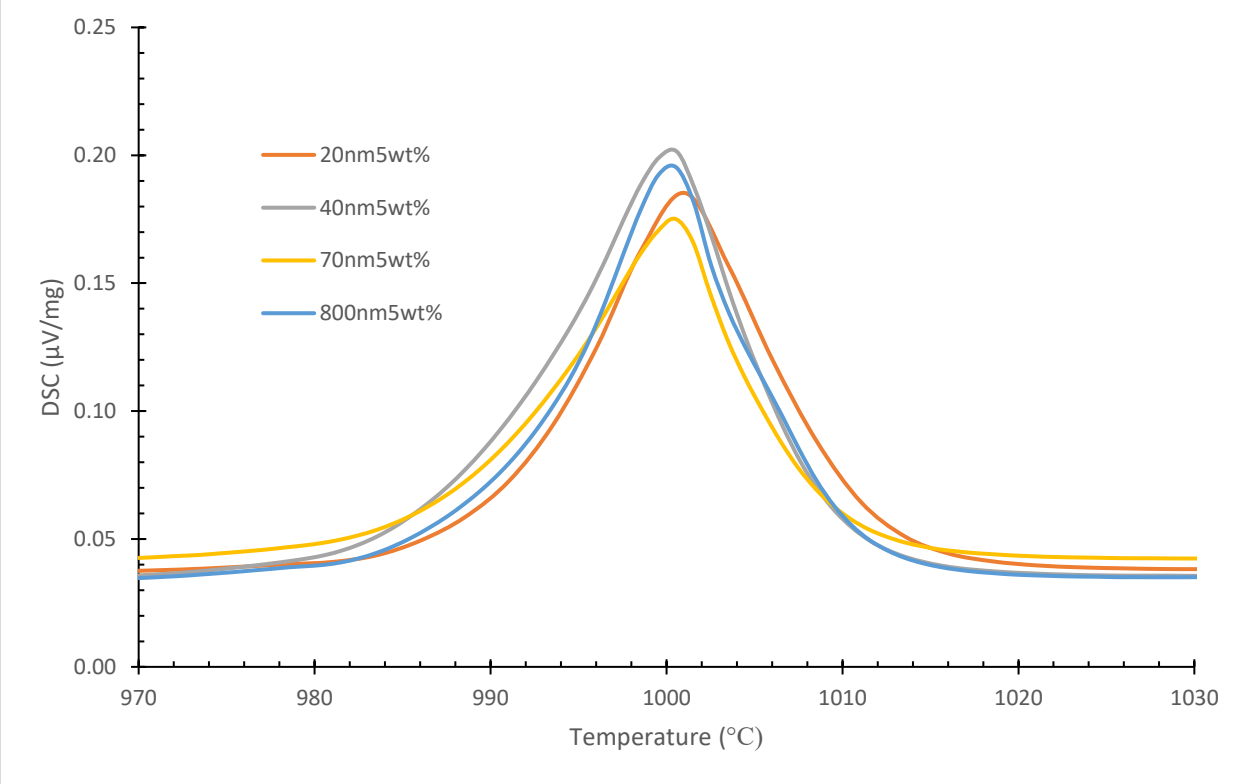

Figure 16 - Endothermic heating events, melting, of the 5 wt% modified braze alloys.

Table 1 - Average onset and peak temperatures of the melting events in the 5 wt% samples.

(°C)	Baseline	800 nm 5 wt%	70 nm 5 wt%	40 nm 5 wt%	20 nm 5 wt%
Melting Onset	992.2	990.7	986.5	986.7	989.8
Peak	1001.1	1000.3	1000.7	1000.8	1001.5

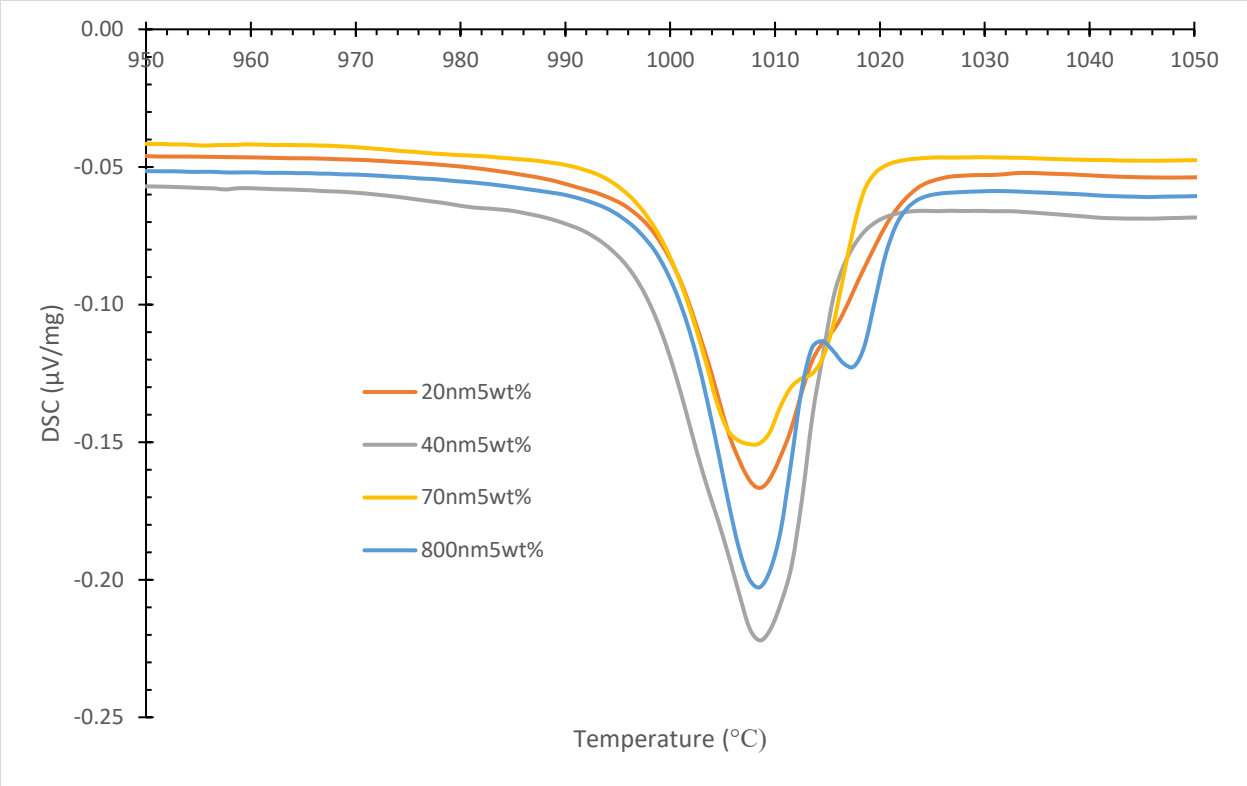

Figure 17 - Exothermic events, solidification, of the 5 wt% modified braze alloys.

Table 2 - Average onset and peak temperatures of the solidification events in the 5 wt% samples.

(°C)	Baseline	800 nm 5 wt%	70 nm 5 wt%	40 nm 5 wt%	20 nm 5 wt%
Solidification Onset	1030.5	1021.8	1019.0	1016.7	1021.7
Liquidus Peak	1025.6	1017.1	1012.2	1008.3	1015.1
Solidus Peak	1011.3	1008.4	1005.4	*	*

*Peak no longer able to differentiate from liquidus.

Table 3 - Difference of average onset and peak temperatures for melting and solidification events from baseline values.

(°C)	Baseline	800 nm 5 wt%	70 nm 5 wt%	40 nm 5 wt%	20 nm 5 wt%
Melting Onset	-	-1.5	-5.7	-5.5	-2.4
Melting Peak	-	-0.8	-0.4	-0.3	0.4
Solidification Onset	-	-8.7	-11.5	-13.8	-8.8
Sol. Liquidus Peak	-	-8.5	-13.4	-17.3	-10.5
Sol. Solidus Peak	-	-2.9	-5.9	*	*

*Peak no longer able to differentiate from liquidus.

Results for the melting event determined through DSC measurements, the onset temperatures and enthalpy, can be found in Figure 18 and Figure 19, respectively. As can be seen, the onset temperature of melting generally increases logrithmically with increasing additive particle size, though the 5 wt% 20 nm series does not follow this trend. Removing the 5 wt% 20 nm series creates better agreement in the remaining data. This can be determined by residual calculations shown by the R^2 value. The calculated melting enthalpy does not show to significantly interact with particle size at a 5 wt% modified braze alloy. It has also been noticed in the baseline series a second peak may be overlapping the primary peak around 1010°C.

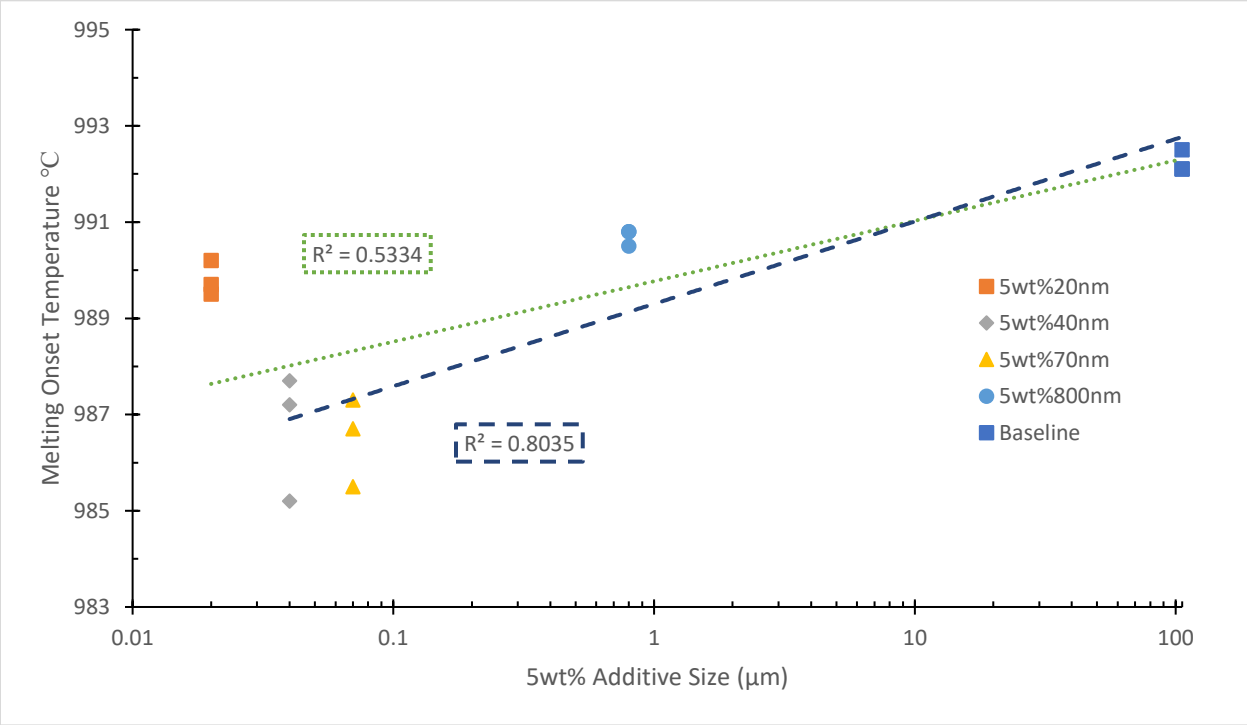

Figure 18 - Onset melting temperature for 5 wt% modified braze alloys. The green dotted trendline represents all data. The blue dashed trendline excludes the 20 nm 5 wt% data.

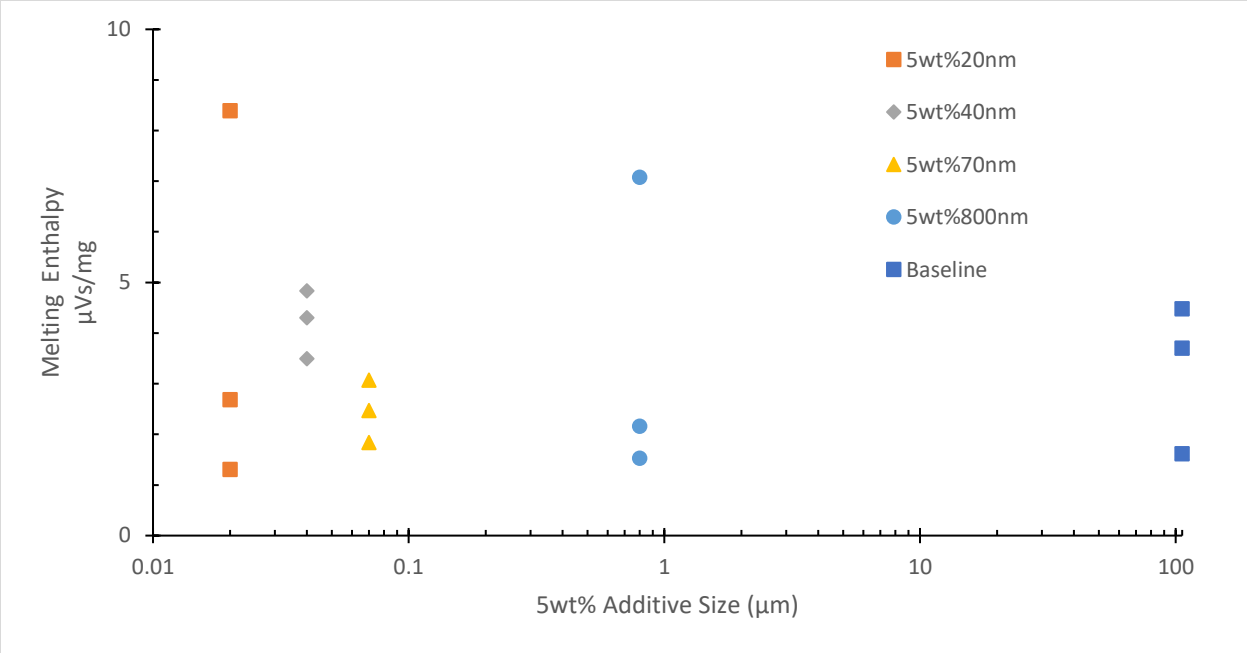

Figure 19 - Melting enthalpy for the 5 wt% modified braze alloys. Enthalpy does not show to significantly differ with particle additive size at 5 wt%.

Results for the solidification event determined through DSC measurements, the onset temperatures and enthalpy, can be respectively found in Figure 20 and Figure 21. Both of which follow the same trends as the melting event. The solidification onset generally increases logarithmically with additive particle size, except for the 5 wt% 20 nm sample that does not follow the trend. Again, this is shown by the residual calculation of the R^2 value. In the same manner as the melting enthalpy, the solidification enthalpy does not show to be significantly affected by additive particle size at 5 wt% modified braze alloy.

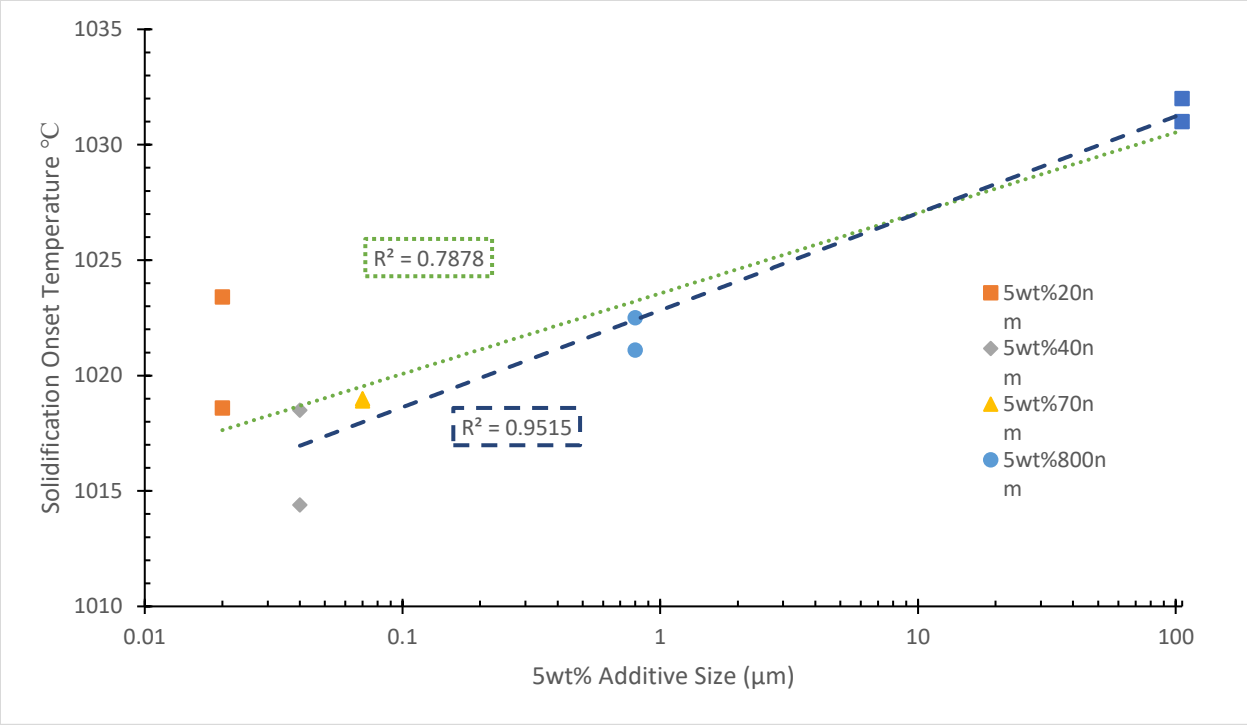

Figure 20 - Onset solidification temperature for 5 wt% modified braze alloys. The green dotted trendline represents all data. The blue dashed trendline excludes the 20 nm 5 wt% data.

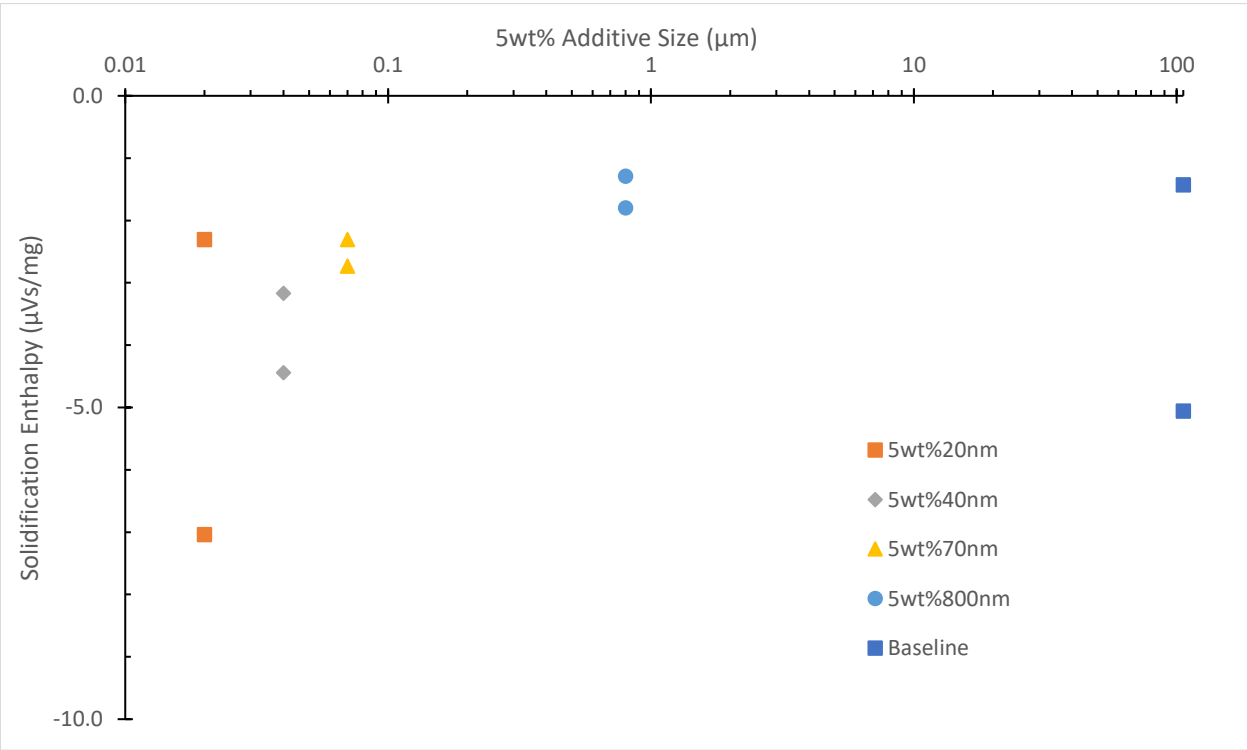

Figure 21 - Solidification enthalpy for the 5 wt% modified braze alloys.

3.2 Influence of increasing Ni nanoparticle additive weight percent

The DSC results for the second series of samples, increasing wt% of 40 nm Ni modified braze alloy, can be found in Figure 22 and Figure 23, the melting and solidification events respectively. As can be seen, the melting and solidification events both drastically change with an increasing amount of Ni NP additive. In the case of melting, the area under the event, or enthalpy, greatly reduces and begins skewing to the left. A second peak can be seen in the 20 wt% 40 nm sample that is not immediately present in any other sample. It should be noted that the peak temperature of melting of the modified braze alloy did not change with increasing wt% of Ni NP additive. During solidification the 20 wt% 40 nm and 5 wt% 40 nm samples lose the bimodal distribution of the baseline and the 20 wt% 40 nm sample skews to the left. A small peak can be seen just below 1050°C in all samples but the baseline. The 40 wt% 40 nm sample loses all the characteristics of the other samples in this series. To better understand the 40 wt% 40 nm sample, Figure 24 shows each of the three runs used to determine results. The 40 wt% 40 nm samples show multiple distinct peaks with the main solidus and liquidus peaks called out. Additional peaks are believed to be intermetallic phases and will be ignored. Table 4 shows the average of the peaks and onsets along with average enthalpy.

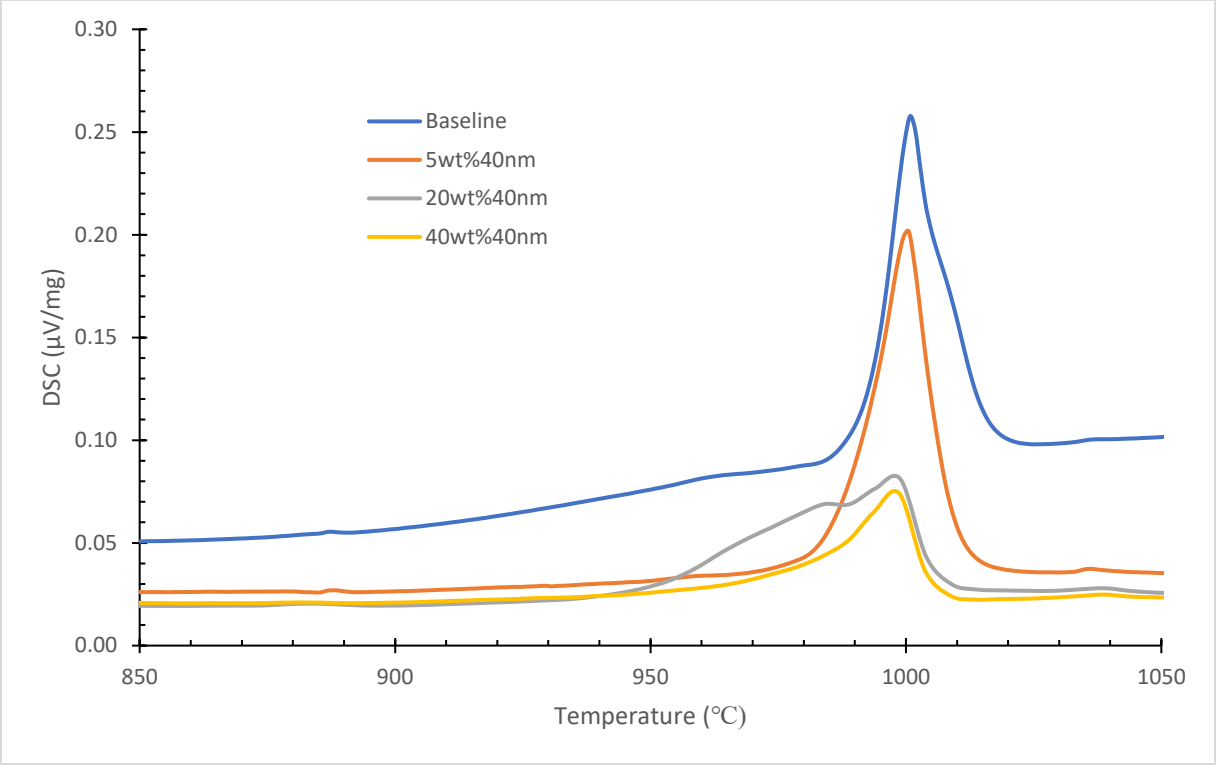

Figure 22 - DSC results of the melting events for increasing wt% of 40 nm Ni modified braze alloy.

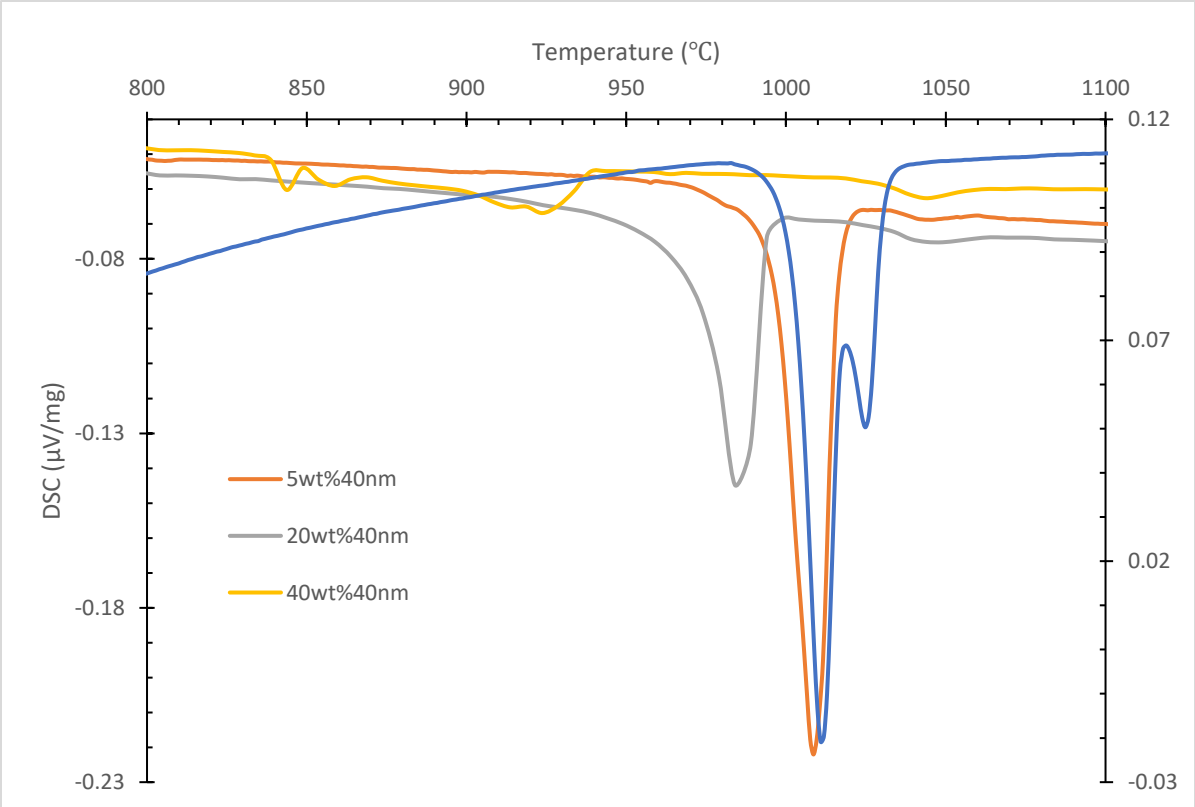

Figure 23 - DSC results of the solidification events for increasing wt% of 40 nm Ni modified braze alloy. Baseline moved to secondary axis to better visually compare results.

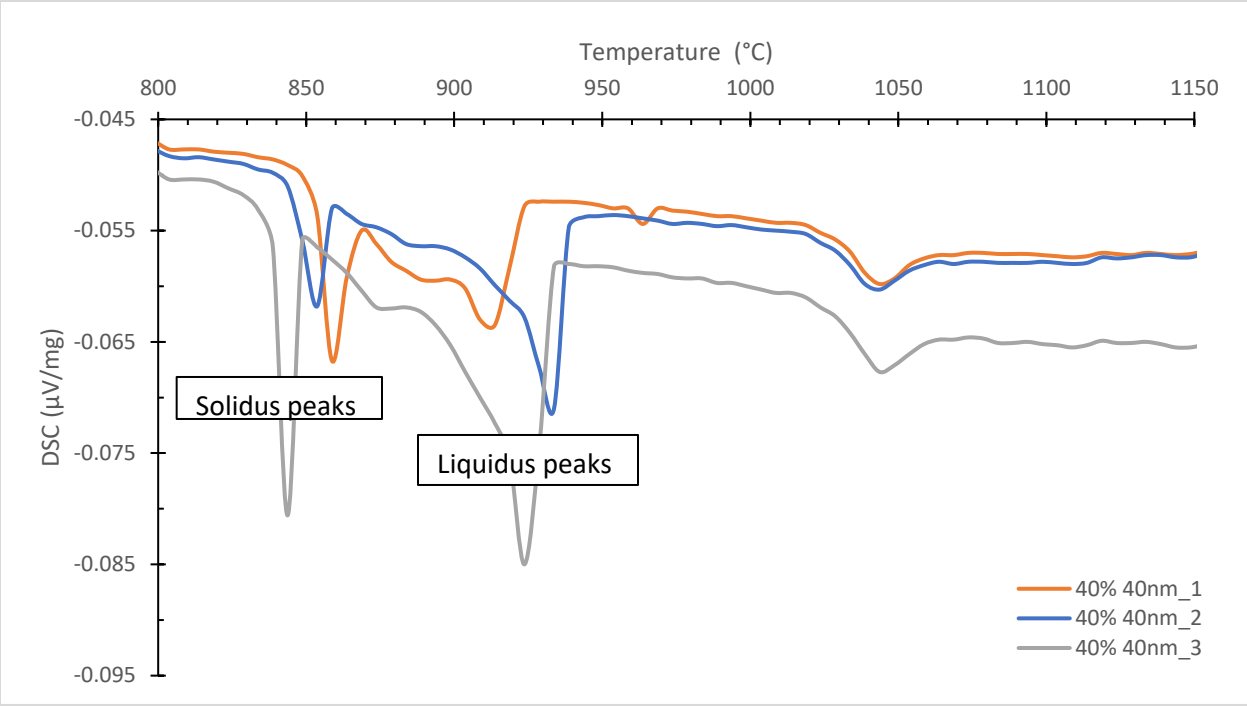

Figure 24 - DSC results of the solidification event for 40 wt% 40 nm Ni modified braze alloy along with peak identification.

Table 4 – Average onset temperature, peak temperature, and enthalpy of the 40 wt% 40 nm samples.

(°C)	1st Peak Onset	1st Peak	2nd Peak	3rd Peak Onset	3rd Peak	Enthalpy (µVs/mg)
40wt%40nm	931	923	884	856	852	-1.2

Figure 25 and Figure 26 show the plotted results of melting and solidification enthalpies from the second series of runs. In both cases, increasing the wt% of 40 nm additive to the modified braze alloy decreased the enthalpy of the heating event. Although, the baseline sample does not look to follow this trend with measured enthalpy values spanning much of the range of the modified braze alloy values.

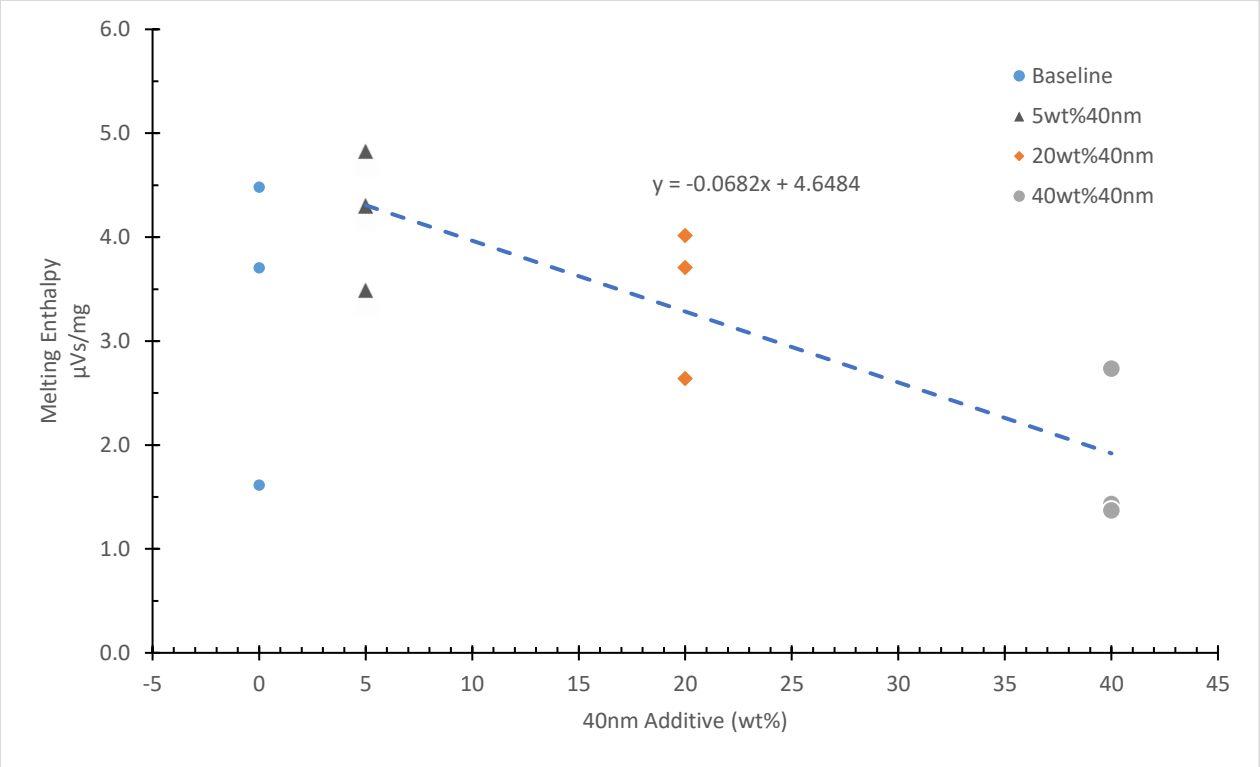

Figure 25 - Melting enthalpy of modified braze alloys with increasing wt% of 40 nm additive. Trendline and equation does not include baseline data.

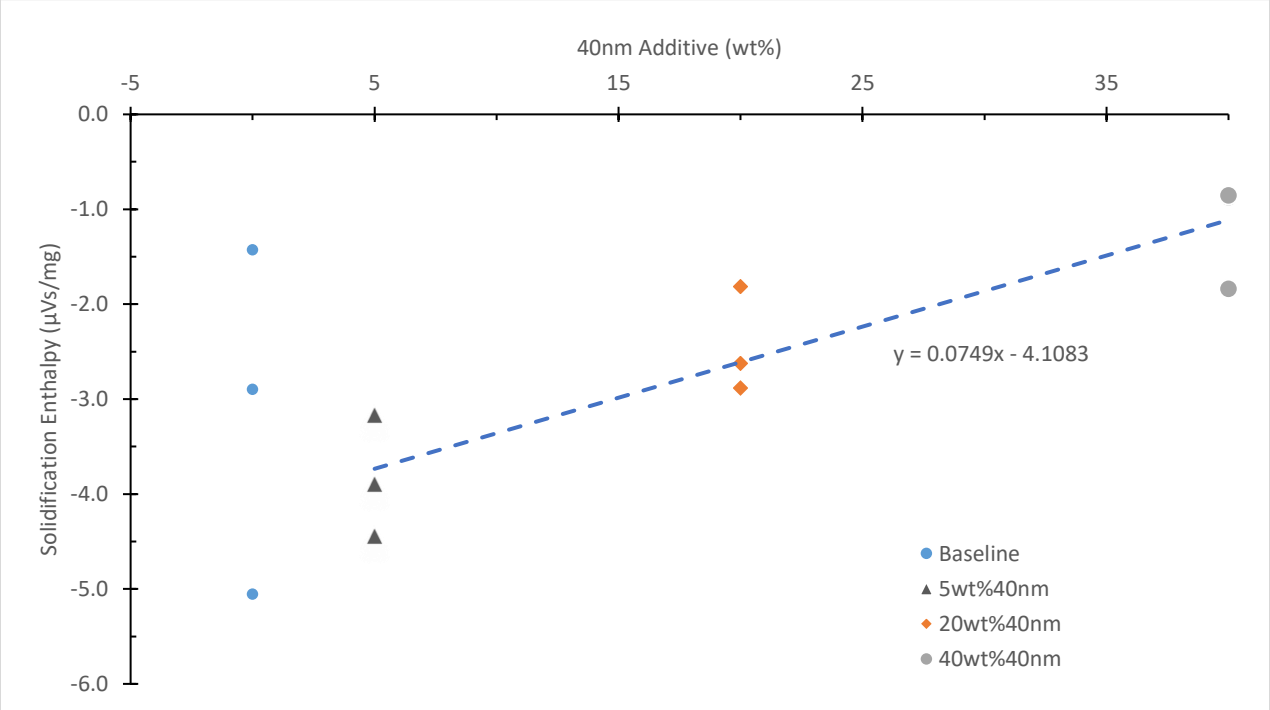

Figure 26 - Solidification enthalpy of modified braze alloys with increasing wt% of 40 nm additive. Trendline and equation does not include baseline data.

It was seen that the first solidification onset temperature of the modified braze alloys decreased linearly with the increase in wt% of the 40 nm NP additive. At a rate of approximately -2.42 °C/wt% Ni additive. These results are plotted in Figure 27. Determining the onset temperature of the melting event for these same samples has proven difficult. As seen in Figure 22, the DSC results for the 20 wt% 40 nm and 40 wt% 40 nm series are left skewed and do not present a clear onset temperature for the Proteus software to determine. Figure 28 shows the results calculated by the analysis software for the melting temperature of the 40 nm additive set of samples. It can be seen the results do not follow a clear trend as was expected.

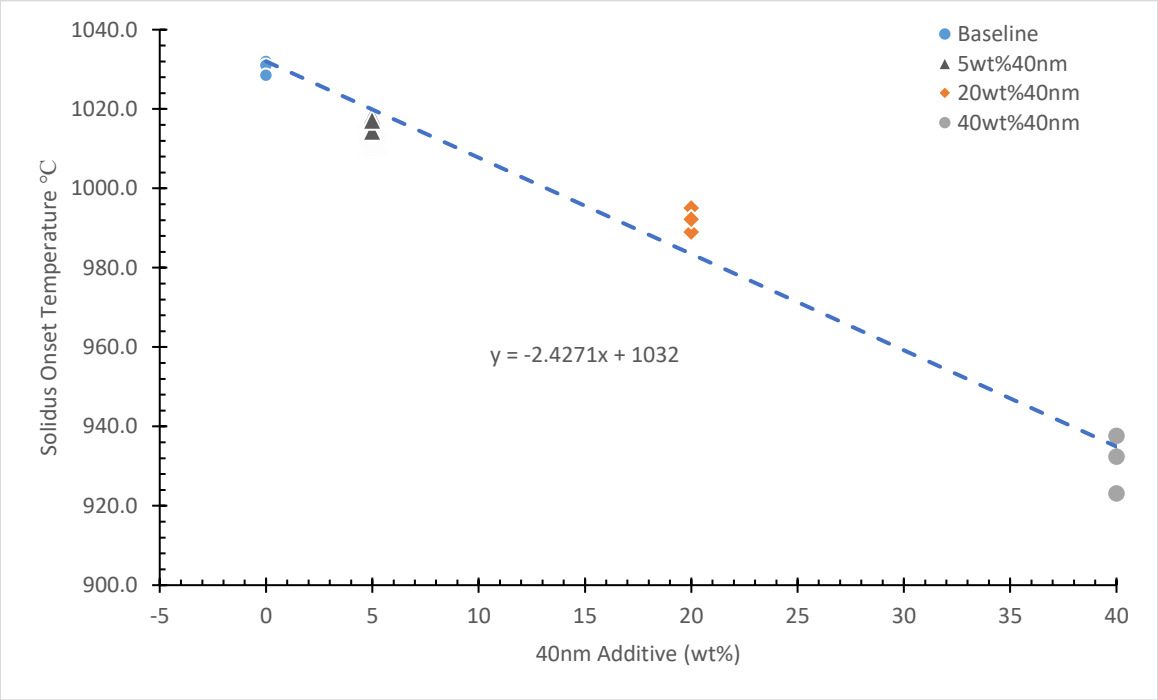

Figure 27 - Initial onset temperature of the solidification event for increasing wt% of 40 nm NP additive in the modified braze alloy.

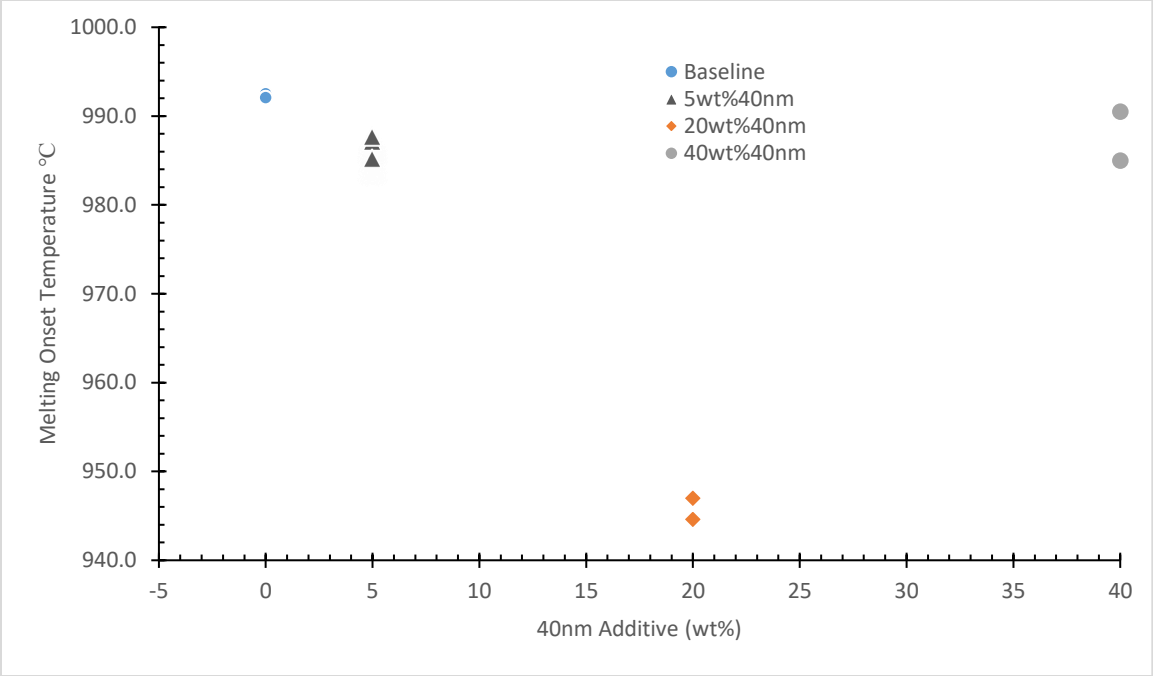

Figure 28 - Initial onset temperature of the melting event for increasing wt% of 40 nm NP additive in the modified braze alloy as determined by the analysis software.

This difference in the results was first believed to be due to the shortened and widened shape of the melting event and an inability for the Proteus software to account for the more gradual shape of the series containing a larger wt% of NPs. For example, Proteus calculates the baseline series onset temperature to be 992°C, shown by a vertical dotted line in Figure 28, which has a derivative at that temperature of 0.008 µV/mg/°C. Neither the 20 wt% 40 nm sample nor the 40 wt% 40 nm sample ever reach a derivative value of that magnitude, as shown in Figure 29. For the purposes of determining onset temperature a derivative reference value of 0.0006 µV/mg/°C was chosen and is displayed as the horizontal dotted line on Figure 29. This value was chosen as it is the first value of the baseline derivative as it escalates towards the peak temperature. When this reference value was chosen as the new method of determining the onset temperature of the second set of samples the values yielded similar results. A second

derivative also produces similar results. Errors in determining onset temperatures from DSC data are well documented by the National Institute of Standards and Technology. [48]

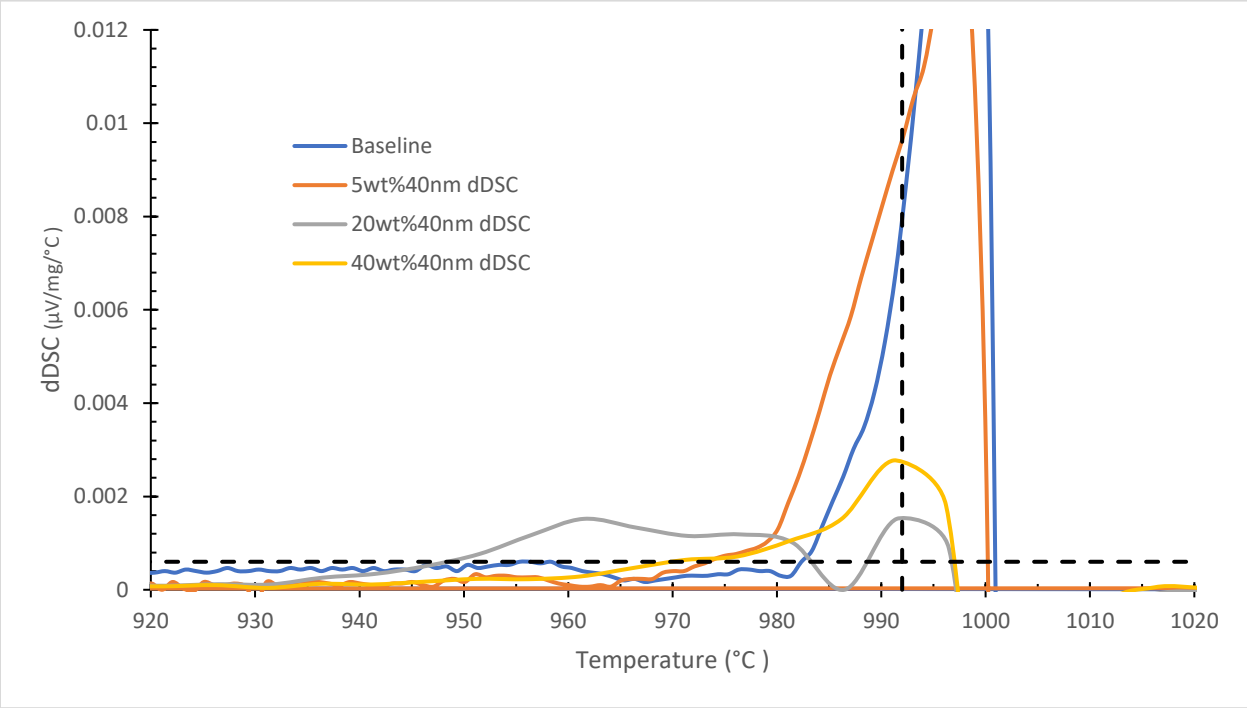

Figure 29 - Derivative of DSC data of the melting events for increasing wt% of 40 nm Ni NP additive with a vertical reference line at 992°C. The horizontal green dotted line is to denote the reference derivative value, 0.0006 µV/mg/°C used for comparison.

3.3 SEM Imagery

SEM images were captured to determine if, due to the lower melting temperature of the Ni NP additives, qualitatively a difference could be detected. Sample micrographs can be seen in Figure 30 and Figure 31 with the lighter braze alloy on the top half and the darker base material on the bottom. The interface line between braze and base metal shows a “cleaner” line with less of the wavy light/dark transition found in the baseline sample.

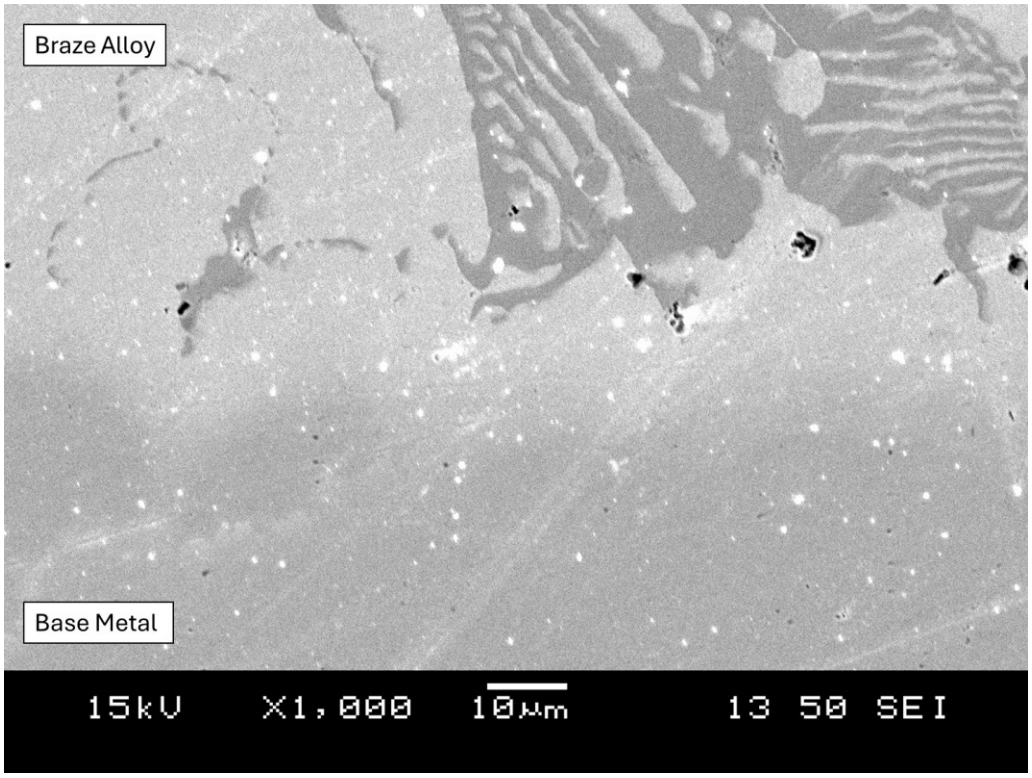

Figure 30 – SEM micrograph of the bonded region in baseline sample with no NP additives.

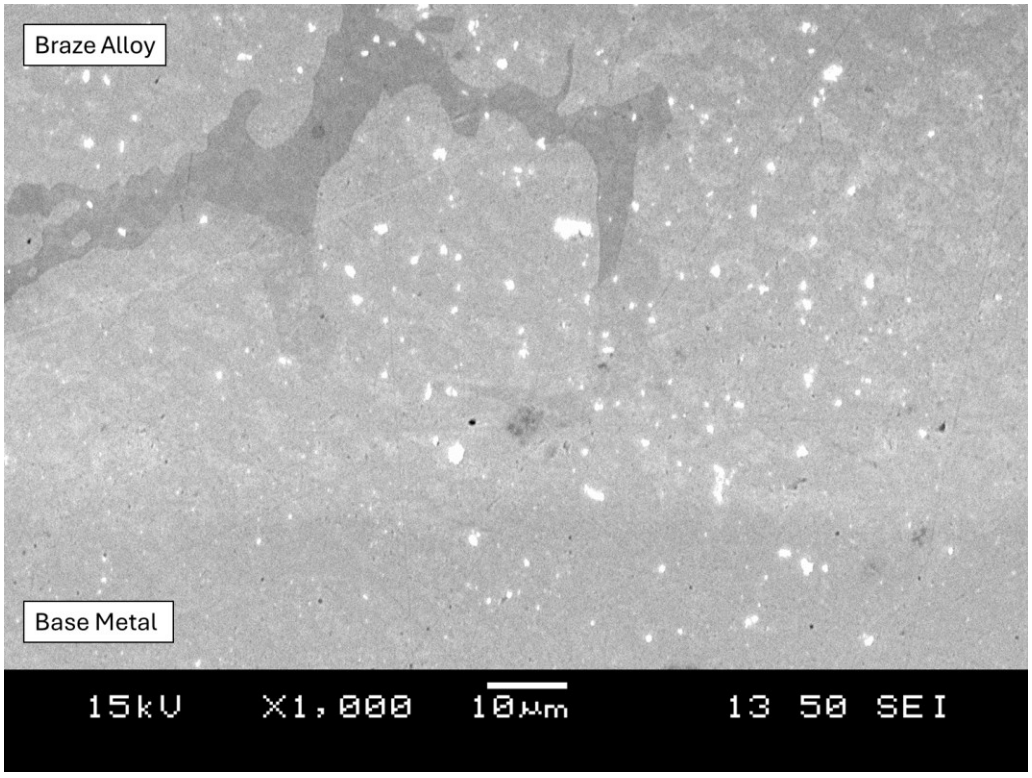

Figure 31 - SEM micrograph of the bonded region in 40 wt% 40 nm Ni NP additive.

Figure 32, Figure 33, and Figure 34 show representative SEM images of the Hoganas BrazeLet Ni613 without any Ni NP additions. As can be seen, particle sizes vary but are generally spherical. Figure 34 shows an individual particle where small imperfections can be seen on the surface but not enough to distort the overall shape or relative smoothness. Figure 35, Figure 36, and Figure 37 show representative SEM images of the 40 wt% 40 nm samples. As can be seen in each figure, the regularity in particle shape is no longer present. Nearly every particle is covered with the Ni NP additive leading to irregularly shaped agglomerates. Figure 35 notes two relatively uncovered Hoganas Brazelet particles for comparison. Figure 38 shows an agglomerate of the 40 nm Ni NPs used in the samples. These images show that while many of the base Hoganas Brazelet Ni613 particles were covered in 40 nm Ni NPs, some base particles remained relatively uncovered and loose Ni NP aggregates existed.

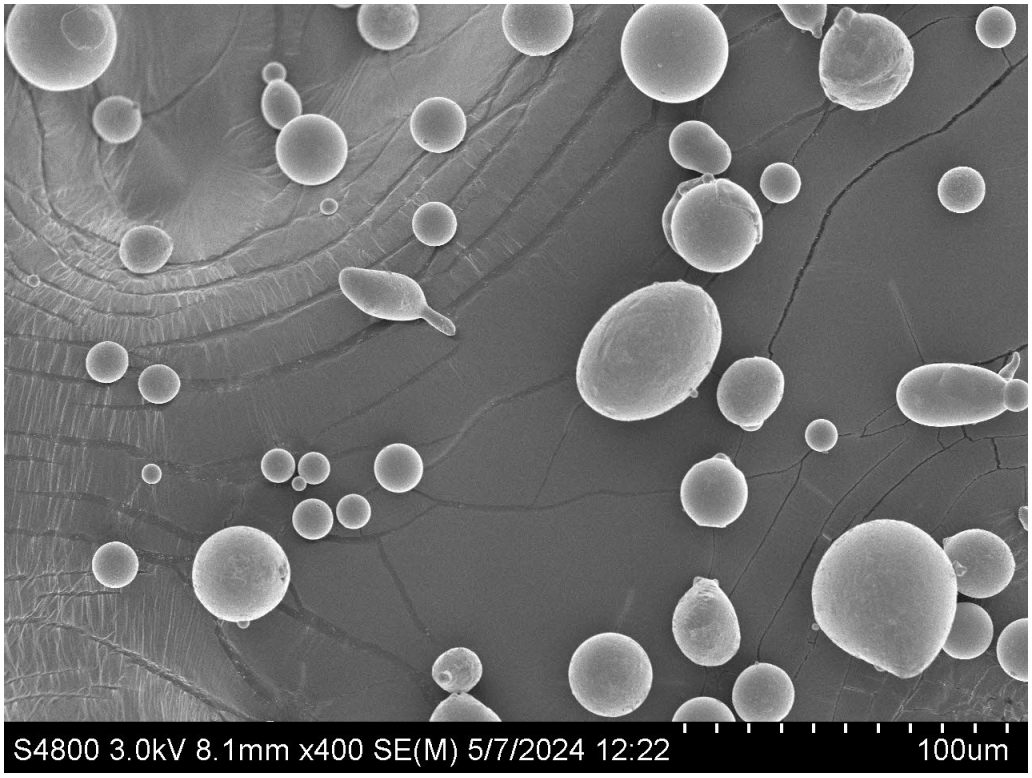

Figure 32 - SEM image of Hoganas Brazelet Ni613 braze alloy particles at 400x magnification.

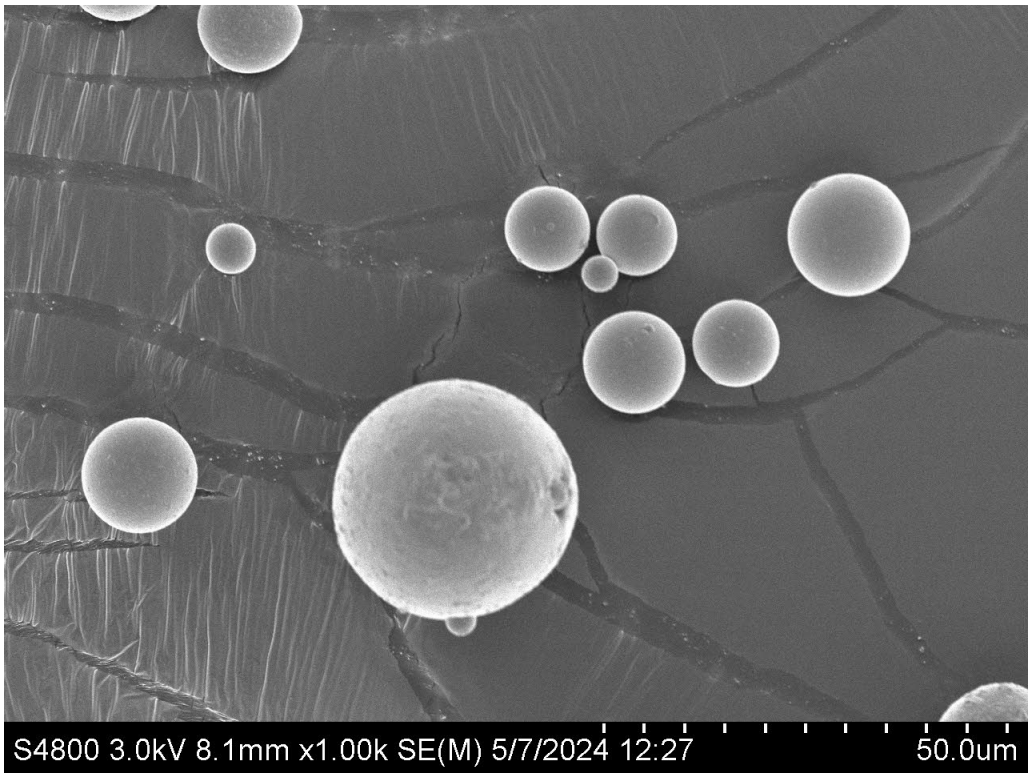

Figure 33 - SEM image of Hoganas Brazelet Ni613 braze alloy particles at 1000x magnification.

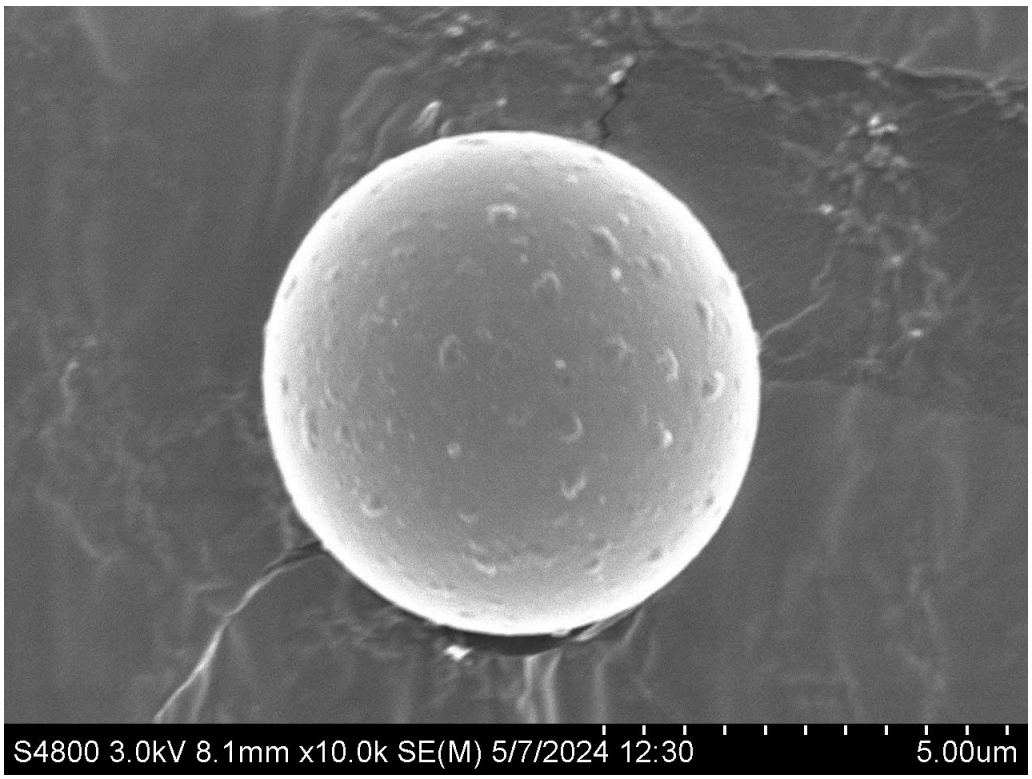

Figure 34 - SEM image of Hoganas Brazelet Ni613 braze alloy particles at 10,000x magnification.

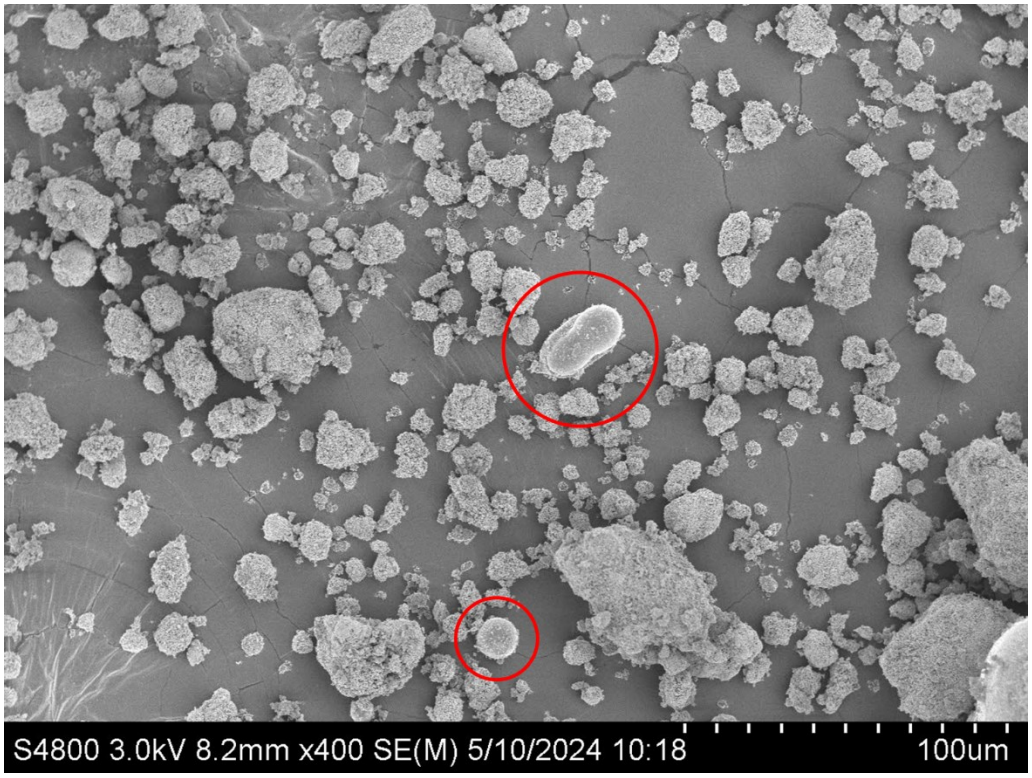

Figure 35 - SEM image of the 40 wt% 40 nm modified braze alloy at 400x magnification. Red circles note two relatively uncovered Hoganas Brazelet Ni613 particles.

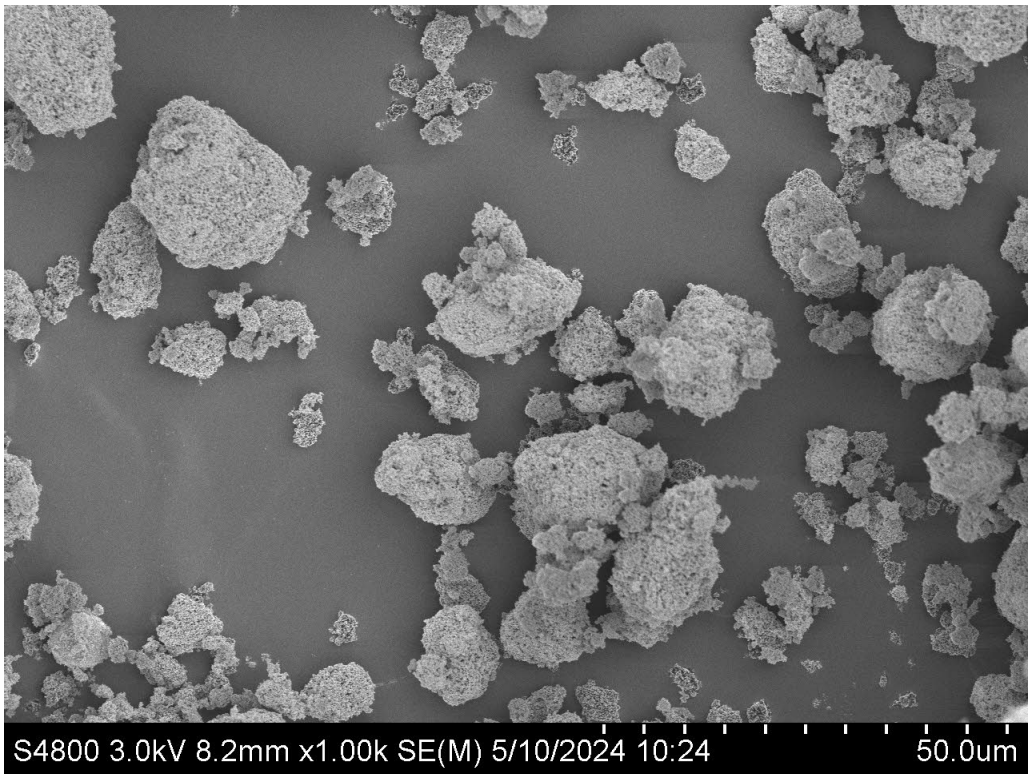

Figure 36 - SEM image of the 40 wt% 40 nm modified braze alloy at 1000x magnification.

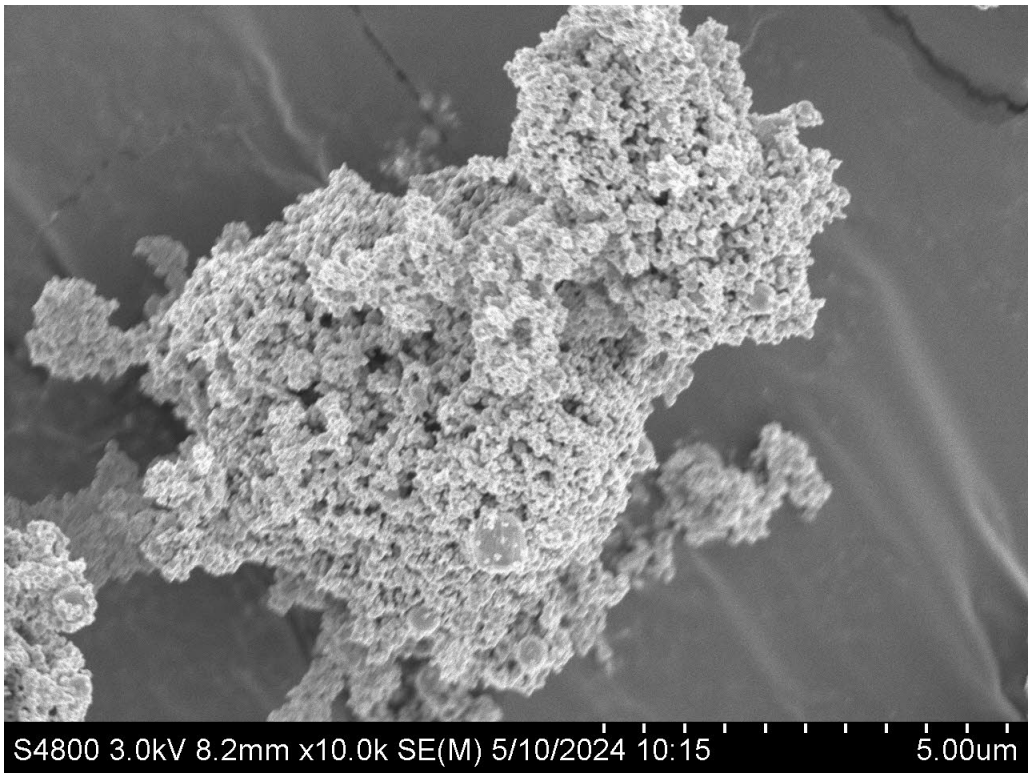

Figure 37 - SEM image of the 40 wt% 40 nm modified braze alloy at 10,000x magnification.

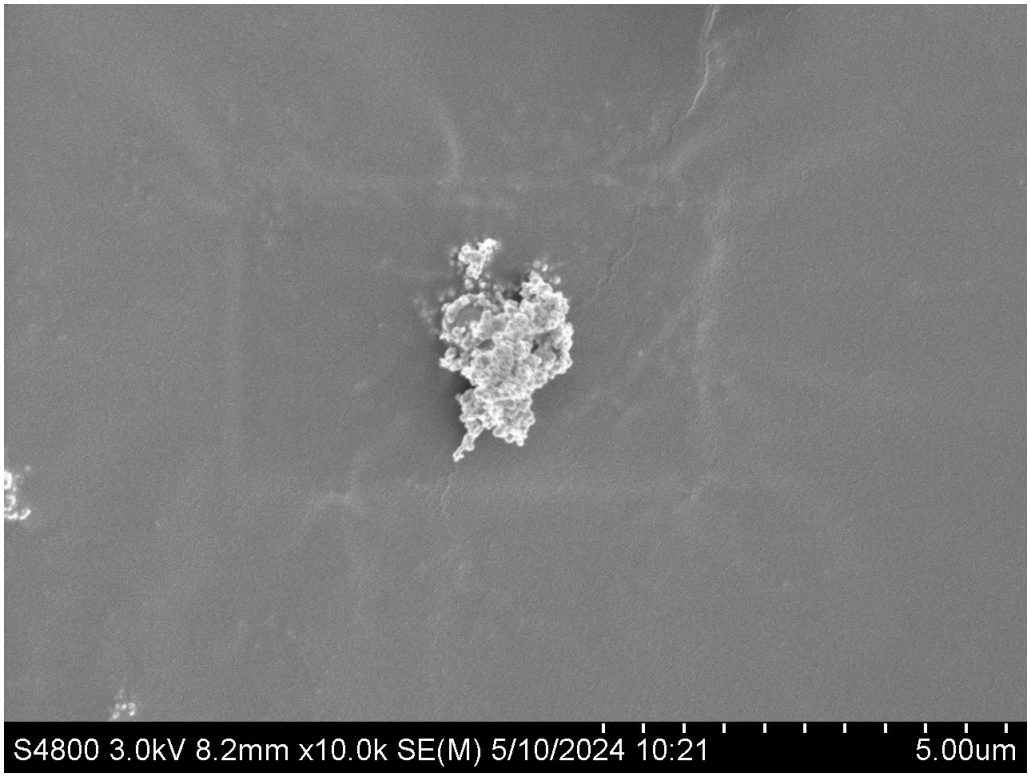

Figure 38 - SEM image of an aggregate of the 40 nm Ni NPs found in the 40 wt% 40 nm braze alloy sample.

4. Discussion

4.1 Influence of increasing Ni additive particle size

As previously discussed above and seen in Figure 18 , the melting temperature tends to decrease as the particle size of the nanoparticles is reduced. This trend is likely due to the increase in interfacial energy of the nanoparticles and generally agrees with the Gibbs-Thomson equation shown in Equation 2. The 20 nm sample does not follow this trend. This is believed to also be due to the higher interfacial energy of the smaller particles. It is likely that the 20 nm particles readily oxidized and agglomerated in atmosphere. Surface oxides raising the melting temperature of NPs is well understood and described in detail by Sun et al. [49]

Figure 39 shows the broken out exothermic solidification peaks of the 5 wt% modified braze alloys. The data suggests as the size of 5 wt% NP additive decreases the first of the two solidification events shifts towards a lower temperature. The two peaks seen in Figure 39A are expected of a eutectic system. The predominant Ni-Cr system, shown in Figure 15, exhibits a narrow α+L region which is further constrained by the presence of Si, B, and P acting as melting point depressants. Figure 39B, showing the 5 wt% 800 nm sample, still behaves similarly to a bulk eutectic system with two distinct peaks. This may be explained by the changes brought about by the smaller additive are not significant enough to more strongly influence the bulk eutectic behavior at 5 wt% of 800 nm. These results may also be explained by the pure Ni 800 nm particles not dissolving fully into solution. As pure nickel has a higher melting temp, regions of solid or semi-solid nickel in the melt would influence the DSC results for solidification. Table 5 shows the average melting and solidification onset values per sample set of Figure 18 and Figure 20, respectively.

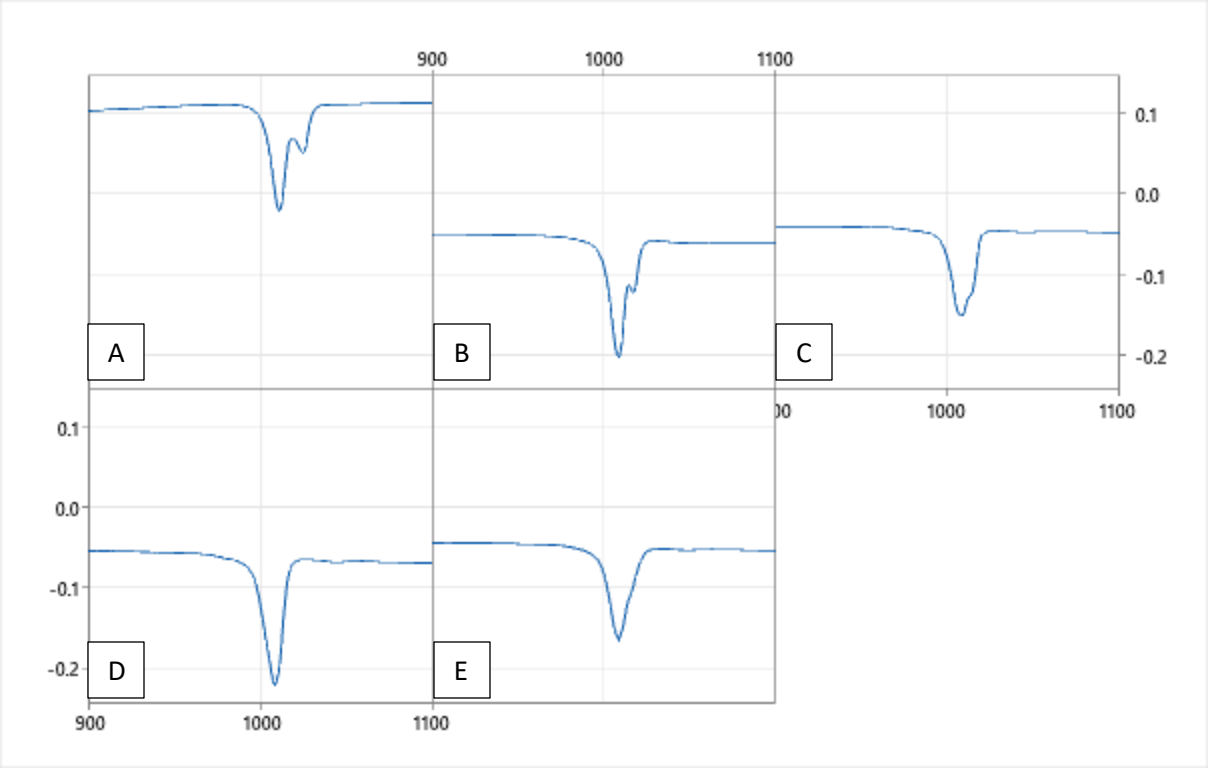

Figure 39 - DSC solidification results 5 wt% modified braze alloys. A: baseline. B: 5 wt% 800 nm. C: 5 wt% 70 nm. D: 5 wt% 40 nm. E: 5 wt% 20 nm.

Table 5 - Influence of particle size on onset melting and solidification average temperatures.

5 wt% Particle Size	20 nm	40 nm	70 nm	800 nm	Baseline
Melting Onset (°C)	989.8	986.7	986.5	990.7	992.2
Solidification Onset (°C)	1021.7	1016.7	1019.0	1021.8	1030.5

While particle size has been shown to affect melting enthalpy [50], 5 wt% nanoparticle is not likely a large enough compositional change to be detectable in this investigation.

4.2 Influence of increasing Ni nanoparticle additive weight percent

In the same manner as decreasing the additive NP size decreases the melting onset temperature of the filler blend, increasing the weight percent of nanoparticle additive decreases the overall melting onset temperature. This changes as more of the filler material is

replaced by the higher interfacial energy nanoparticles, as shown in Table 6. As mentioned in the results section, a comparative value for the onset temperature of the 40 wt% 40 nm samples could not be determined. Inflection points for these samples could be seen as early as 880°C. This generally agrees with the Gibbs-Thomas effect, shown in Equation 2. Figure 40 shows a potential error introduced when determining onset temperatures with DSC. Though these errors are known, this investigation is concerned with general phenomenon and not specific temperatures. Therefore, extrapolated onset temperatures are considered sufficient.

Table 6 - Influence of wt% NP additive on onset melting and solidification average temperatures.

40 nm Additive	Baseline (0 wt%)	5 wt%	20 wt%	40 wt%
Melting Onset (°C)	992.2	986.7	946.2	-
Solidification Onset (°C)	1030.5	1016.7	992.1	931.0

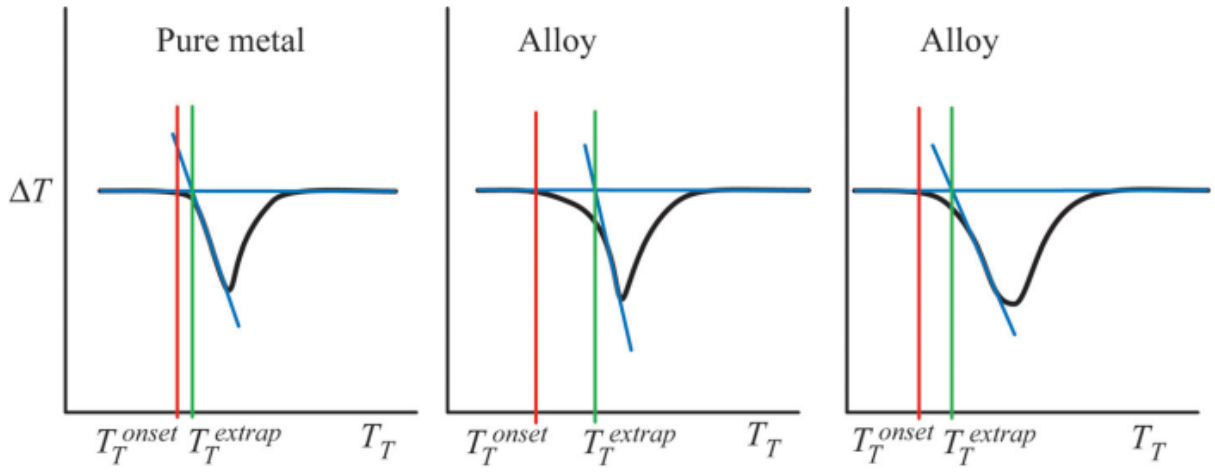

Figure 40 - Schematic DTA plots showing error introduced by using the extrapolation method for onset determination rather than the first detectable departure from baseline. [48]

Table 6 also notes the decrease in solidification temperature due to the increase in Ni NP additive. As discussed in the introduction and shown in Figure 8, within eutectic systems the phase boundaries tend to shift to lower temperatures as the nominal particle size of the system

also decreases. A similar phenomenon is believed to be happening in all samples but becomes clear in the 40 wt% 40 nm samples. Figure 41 shows this effect schematically. It should also be noted that the %Ni in the system drastically increases from the base alloy. This increase in Ni would move the overall composition away from the eutectic composition and should show an increase in the solidification temperature yet it is believed any increase due to compositional changes are overshadowed by the massive decrease in average particle size of the system. The change in composition, ignoring melting point depressants, is shown in Table 7. The amount of melting point depressants within the system, though significantly reduces the melting and solidification temperatures, are not investigated in further detail outside of this known effect.

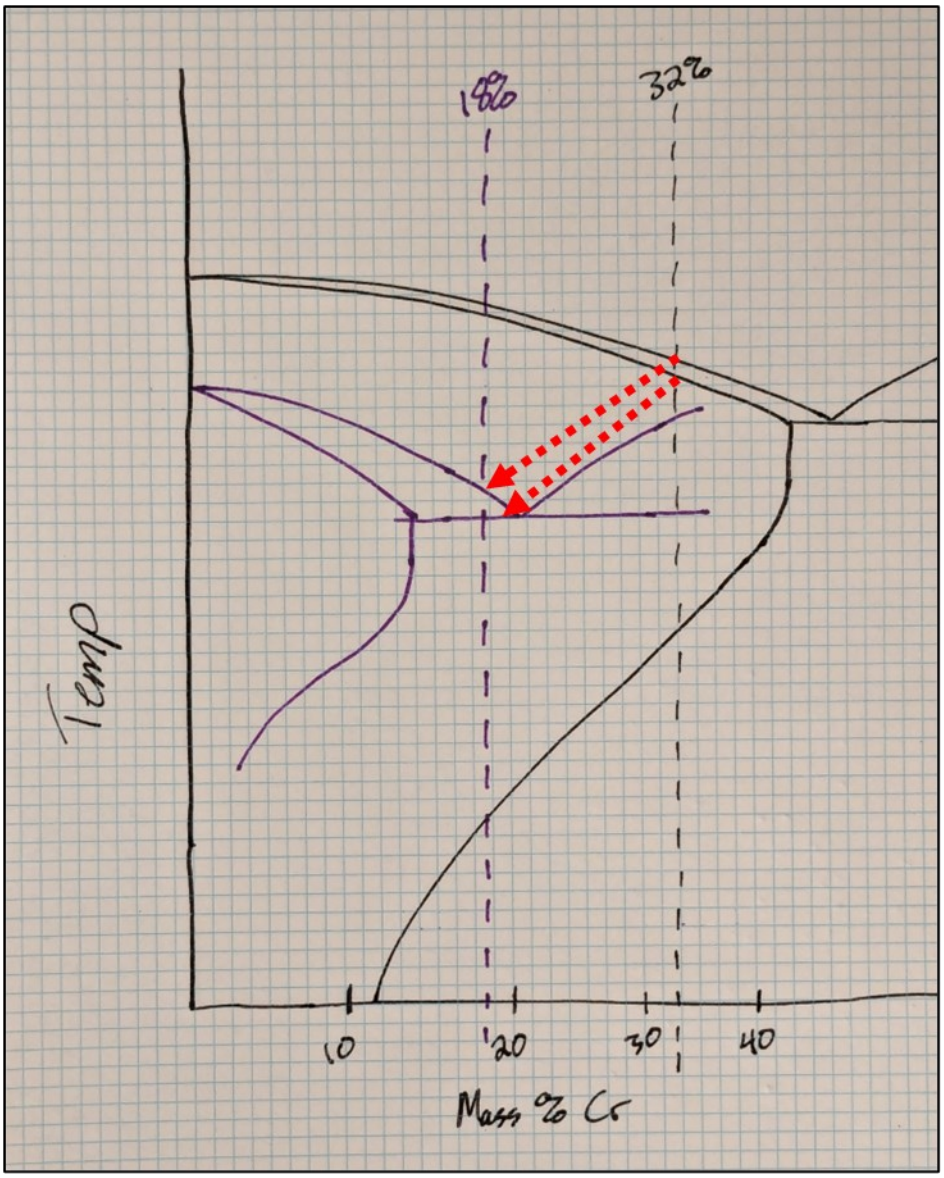

Figure 41 - Schematic showing the shift in the Ni-Cr phase diagram believed to be happening with the 40 wt% 40nm samples. Showing how the eutectic point and composition have moved closer together. Not drawn to scale.

Table 7 - Change in Ni-Cr composition of 40 nm Ni additive samples. Melting point depressents ignored.

Comp. wt% (ignoring MPD)	Ni	Cr
Hoganas Brazelet Ni613	68	32
5 wt% Ni additive	69	31
20 wt% Ni additive	75	25
40 wt% Ni additive	82	18

While increasing the weight percent of NPs in the system decreased the enthalpy of each thermal event, as expected, the baseline sample does not follow this same trend. This is believed to be due to local inhomogeneity within each sample.

5. Conclusion

The results of decreasing the 5 wt% Ni additive particle size showed a detectable decrease in the melting and solidification temperature of the modified braze alloy. Although not large, around 5°C for melting and 15°C for solidification with the 5 wt% 40 nm sample, this result was expected and does agree with general knowledge. Melting and solidification temperature is directly proportional to particle size. At only 5 wt% NP additive, the effects on enthalpy could not be measured in this investigation.

Increasing the quantity of the NP additive up to 40 wt% decreased the melting temperature by a detectable 112°C. This also decreased the solidification onset temperature by 100°C. Not including the baseline sample, the enthalpy results were shown to decrease in magnitude with the increase in wt% of NPs. It was not determined why the baseline sample does not follow the same trend.

6. Future Work

Future work could conduct a similar experiment to determine the effect of additive particle size on the braze alloy. While the results were statistically different, the magnitude of the effects with only a 5 wt% NP additive were minimal. A larger amount could show a more pronounced effect.

Dissolution depth could not be measured accurately due to the sample setup used. With a more uniform setup and homogenous modified braze alloy, careful measurements via SEM-EDS could show the effect of NP additive on dissolution depth. Further work could then be carried out studying the mechanical properties of the resulting bond.

While previous work has shown that sub-10 nm particles can have a drastic effect on melting temperature, particles of this size are difficult to maintain and use. Additionally, melting point depressants can drastically lower the melting point of a braze alloy but are known to result in deleterious brittle phases. A study could be conducted to decrease the nominal size of the entire system, melting point depressants included, to tens of NM. This, ideally, could result in a “best of both worlds” situation, capitalizing on both physical and chemical properties of the material.

References

[1] H. Bian, Y. Song, D. Liu, Y. Lei, X. Song and J. Cao, "Joining of SiO2 ceramic and TC4 alloy by nanoparticles modified brazing filler metal," *Chinese Journal of Aeronautics,* 2019.

[2] T. Zaharinie, F. Yusof, M. Hamdi, T. Ariga and R. Moshwan, "Effect of brazing temperature on the shear strength of Inconel," *The International Journal of Advanced Manufacturing Technology,* vol. 73, pp. 1133-1140, 2014.

[3] A. Sharma, D. E. Xu and J.-P. Jung, "Effect of different nanoparticles on microstructure, wetting and joint strength of Al-12SI-20Cu braze filler," *Materials Research Express,* vol. 6, 2019.

[4] G. J. J.-R. a. L. P. H. J. Kaptay, "Melting point depression and fast diffusion in nanostructured brazing fillers confined between barrier nanolayers," *Journal of Materials Engineering and Performance,* 2016.

[5] L. Somlyai-Sipos, D. Janovszky, A. Sycheva and P. Baumli, "Investigation of the Melting Point Depression of Copper," *IOP Conference Series: Materials Science and Engineering,* 2020.

[6] T. S. Akhtar, K. O. Cooke, T. I. Khan and M. A. Shar, "Nanoparticle Enhanced Eutectic Rreaction during Diffusion Brazing of Aluminum to Magnesium," *Nanomaterials,* vol. 9, no. 370, 2019.

[7] M. Yeh and T. Chuang, "Effects of Applied Pressure on the Brazing of Superplastic INCONEL 718 Superalloy," *Metallurgical and Materials Transactions,* vol. 28, no. a, pp. 1367-1376, 1997.

[8] K. Bobzin, Ö. Mehmet and W. Stefanie, "Investigation of the effect of contaminations and cleaning processes on the surface properties of brazing surfaces," *IOP Conference Series: Materials Science and Engineering,* vol. 181, no. 1, 2017.

[9] H. Nayeb-Hashemi and M. Lockwood, "The effect of processing variables on the microstructures and properties of aluminum brazed joints," *Journal of Materials Science,* vol. 37, pp. 3705-3713, 2002.

[10] B. Ahn, "Recent Advances in Brazing Fillers for Joining of Dissimilar Metals," *Metals,* vol. 11, no. 7, 2021.

[11] D. Bridges, "Wettability, Diffusion Behaviors, and Modeling of Ni Nanoparticles and Nanowires in Brazing Inconel 718," *Advanced Engineering Materials,* 2021.

[12] K. Ikeuchi, Y. Zhou, H. Kokawa and T. North, "Liquid-Solid Interface Migration at Grain Boundary," *Metallurgical Transactions A,* vol. 23A, pp. 2905-2915, 1992.

[13] E. Hedin, "Influence of Gap Clearance on Brazing Joint Strength for Ni and Fe Based Filler," in *IBSC*, New Orleans, 2018.

[14] International Stainless Steel Forum, "Stainless Steel in Figures 2020," [Online]. Available: https://www.worldstainless.org/Files/issf/non-image-files/PDF/ISSF_Stainless_Steel_in_Figures_2020_English_public_version.pdf. [Accessed 10 November 2023].

[15] S. Mishra, A. Sharma, D. H. Jung and J. P. Jung, "Recent Advances in Active Metal Brazing of Ceramics and Process," *Metals and Materials International,* vol. 26, pp. 1087-1098, 2020.

[16] W. Guo, T. Wang, T. Lin, S. Guo and P. He, "Bismuth borate zinc glass braze for bonding sapphire in air," *Materials Characterization,* vol. 137, pp. 67-76, 2018.

[17] A. Inoue, "Stabilization of metallic supercooled liquid and bulk amorphous alloys," *Acta materialia,* vol. 48, no. 1, pp. 279-306, 2000.

[18] J. Kim and T. Lee, "Brazing method to join a novel Cu54Ni6Zr22Ti18 bulk metallic glass," *Science and Technology of Welding and Joining,* vol. 22, no. 8, pp. 714-718, 2017.

[19] D. Bridges, A. Hu and R. Xu, "Transient Liquid Phase Bonding of Inconel 718 with Ni and BNi-2 Nano-Braze Materials," *International Manufacturing Science and Engineering Conference,* vol. 58752, 2019.

[20] R. Eluri and Paul Brian, "Hermetic joining of 316L stainless steel using a patterned nickel nanoparticle," *Journal of Manufacturing Processes,* vol. 14, no. 4, pp. 471-477, 2012.

[21] B. Lehmert, J. Janczak-Rusch, G. Pigozzi, P. Zuraw, F. La Mattina, L. Wojarski, W. Tillmann and L. P. H. Jeurgens, "Copper-Based Nanostructured Coatings for Low-Temperature Brazing Applications," *Materials Transactions,* vol. 56, no. 7, pp. 1015-1018, 2015.

[22] G. Kaptay, J. Janczak-Rusch and L. P. Jeurgens, "Melting Point Depression and Fast Diffusion in Nanostructured Brazing Fillers Confined Between Barrier Nanolayers," *Journal of Materials Engineering and Performance,* vol. 25, pp. 3275-3284, 2016.

[23] J. Jeevanandam, A. Barhoum, Y. S. Chan, A. Dufresne and M. K. Danquah, "Review on nanoparticles and nanostructured materials: history, sources, toxicity and regulations," *Beilstein Journal of Nanotechnology,* pp. 1050-1074, 2018.

[24] Y. Li, Z. Chen, R. Zhou and e. al., "Design of advanced porous silver powder with high-sintering activity to improve silicon solar cells.," *Nano Research,* pp. 1-9, 2023.

[25] M. C. Halbig, B. P. Coddington, R. Asthana and M. Singh, "Characterization of silicon carbide joints fabricated using SiC particulate-reinforced Ag–Cu–Ti alloys," *Ceramics International,* vol. 39, no. 4, pp. 4151-4162, 2013.

[26] W. Hu, S. Xiao, J. Yang and Z. Zhang, "Melting evolutiona dn diffusion behavior of vanadium nanoparticles.," *The European Physical Journal,* vol. 45, pp. 547-554, 2005.

[27] P. Pawlow, "Über die Abhängigkeit des Schmelzpunktes von der Oberflächenenergie eines festen Körpers. [On the dependence of the melting point on the surface energy of a solid body.]," *Zeitschrift für physikalische Chemie [Journal of Physical Chemistry],* vol. 65, no. 1, pp. 1-35, 1909.

[28] K. K. Nanda, "Size-dependent melting of nanoparticles: Hundred years of thermodynamic model," *Pramana,* vol. 72, no. 4, pp. 617-628, 2009.

[29] K. Sattler, "Handbook of Nanophysics: Functional Nanomaterials," in *Handbook of Nanophysics*, CRC Press, 2010, p. 2.9.

[30] M. Salmaliyan and M. Shamanian, "Formation mechanism of intermetallic components during dissimilar bonding in IN718/BNi-2/AISI316 by TLP process," *Heat and Mass Transfer,* vol. 55, pp. 2083-2093, 2019.

[31] X. J. Yuan, M. B. Kim and C. Y. Kang, "Effects of boron and silicon on microstructure and isothermal solidification during TLP bonding of a duplex stainless steel using two Ni–Si–B insert alloys," *Materials Science and Technology,* vol. 27, no. 11, pp. 1191-1197, 2011.

[32] S. Tung, L. Lim and M. Lai, "Solidification phenomena in nickel base brazes containing boron and silicon.," *Scripta Materialia,* vol. 34, no. 5, pp. 763-769, 1996.

[33] A. Ghasemi and M. Pouranvari, "Intermetallic phase formation during brazing of a nickel alloy using a Ni-Cr-Si-B quinary filler alloy.," *Science and Technology of Welding and Joining,* vol. 24, no. 4, pp. 342-351, 2019.

[34] M. Pouranvari, A. Ekrami and A. H. Kokabi, "Role of base-metal composition in isothermal solidification during diffusion brazing of nickel-based superalloys," *Science and Technology of Welding and Joining,* vol. Vol. 23, no. No. 1, pp. 13-18, 2018.

[35] T. K. Santosh, *Nickel nanoparticles-assisted diffusion brazing of stainless steel 316 for microfluidic applications.,* Oregon State University, 2010.

[36] W. Tillmann, T. Ulitzka, L. Wojarski, M. Manka, H. Ulitzka and D. Wagstyl, "Development of high entropy alloys for brazing applications," *Welding in the World,* vol. 64, pp. 201-208, 2020.

[37] D. Bridges, S. Zhang, S. Lang, M. Gao, Z. Yu, Z. Feng and A. Hu, "Laser Brazing of a Nickel-based Superalloy using a Ni-Mn-Fe-Co-Cu," *Materials Letters,* vol. 215, pp. 11-14, 2018.

[38] S. K. Tiwari and B. K. Paul, "Comparison of Nickel Nanoparticle-Assisted DIffusion Brazing of Stainless Steel to Conventional Diffusion Brazing and Bonding Processes," *Journal of Manufacturing Science and Engineering,* vol. 132, no. 030902, pp. 1-5, 2010.

[39] M. Wautelet, J. P. Dauchot and M. Hecq, "Phase diagrams of small particles of binary systems: a theoretical approach," *Nanotechnology,* vol. 11, pp. 6-9, 2000.

[40] J. Sopoušek, J. Vřešťál, A. Zemanova and J. Bursik, "Phase diagram predictio and particle characterization of Sn-Ag nano alloy for low metling point lead-free solders.," *Journal of Mining and Metallurgy, Section B: Metallurgy,* vol. 48, no. 3, pp. 419-425, 2012.

[41] A. Roshanghias, J. Vrestal, A. Yakymovych, K. Richter and H. Ipser, "Sn–Ag–Cu nanosolders: Melting behavior and phase diagram prediction in the Sn-rich corner of the ternary system.," *CALPHAD,* vol. 49, pp. 101-119, 2015.

[42] H. G. Kim, J. Lee and G. Makov, "Phase diagram of binary alloy nanoparticles under high pressure," *Materials,* vol. 14, p. 2929, 2021.

[43] B. J. Kim, J. Tersoff, C.-Y. Wen, M. C. Reuter and E. A. Stach, "Determination of Size Effects during the Phase Transition of a Nanoscale Au-Si Eutectic," *Birck and NCN Publications,* vol. Paper 494, 2009.

[44] G. Kumar, A. Sharma, S. Kashyap, Z. Beddiaf and C. Shekhar, "Thermodynamic modeling of Al-Si nanoalloy phase diagram," *Journal of Nanoparticle Research,* vol. 23, p. 245, 2021.

[45] A. Sharma and B. Ahm, "Brazeability, Microstructure, and Joint Characteristics of ZrO2/Ti-6Al-4V Brazed by Ag-Cu-Ti Filler Reinforced with Cerium Oxide Nanoparticles," *Advances in Materials Science and Engineering,* vol. 2019, pp. 1-11, 2019.

[46] M. L. Kuntz, Y. Zhou and S. F. Corbin, "A Study if Transient Liquid-Phase Bonding of Ag-Cu Using Differential Scanning Calorimetry," *Metallurgical and Materials Transactions,* vol. 37A, pp. 2493-2504, 2006.

[47] R. Eluri and B. Paul, "Silver nanoparticle-assisted diffusion brazing of 3003 Al alloy for microchannel applications," *Materials and Design,* vol. 36, pp. 13-23, 2012.

[48] W. J. Boettinger, U. R. Kattner, K. -W. Moon and J. H. Perepezko, DTA and Heat-flux DSC Measurements of Alloy Melting and Freezing, Washington D.C: National Institute of Standards and Technology, 2006.

[49] J. Sun and S. L. Simon, "The melting behavior of alumin nanoparticles," *Thermochimica Acta,* vol. 463, no. 1-2, pp. 32-40, 2007.

[50] Q. Fu, J. Zhu, Y. Xue and Z. Cui, "Size- and shape-dependent melting enthalpy and entropy of nanoparticles," *Journal of Materials Science,* vol. 52, pp. 1911-1918, 2017.

[51] Hoganas, "BrazeLet® Ni613 Technical Data," May 2013. [Online]. Available: https://www.hoganas.com/en/. [Accessed August 2023].

[52] Wikipedia, "SAE 316L stainless steel," 20 March 2024. [Online]. Available: https://en.wikipedia.org/wiki/SAE_316L_stainless_steel. [Accessed 21 April 2024].

[53] I. Robin, T. Gräning, Y. Yang, S. Haider, E. Lass, Y. Katoh and S. Zinkle, "Evaluation of Tungsten—Steel Solid-State Bonding Options and the Role of CALPHAD to Screen Diffusion Bonding Interlayers," *Metals,* vol. 13, no. 8, p. 1438, 2023.

[54] M. Karthik, J. Abhinav and K. V. Shankar, "Morphological and Mechanical Behaviour of Cu–Sn Alloys—A review," *Metals and MAterials International,* vol. 27, pp. 1915-1946, 2021.

APPENDIX – Composition of Materials and Ni-Cr Phase Diagram

Table 8 - Purity of purchased Ni nanoparticles.

Contaminant (ppm)	800 nm Ni	70 nm Ni	40 nm Ni	20 nm Ni
As	<10	<20	<20	-
Bi	<5	-	-	-
C	-	<1000	<1000	-
Ca	-	-	-	7.1
Cd	<10	-	-	-
Co	<20	-	-	-
Cr	-	-	-	-
Cu	-	<600	<600	5
Fe	-	<1000	<1000	76.9
Hg	<10	-	-	-
K	-	-	-	8.3
Mg	<10	<1000	<1000	12.1
Mn	-	<50	<50	2.5
Na	-	-	-	22.3
P	<10	<20	<20	-
Pb	<10	<20	<20	2.5
S	-	<50	<50	-
Sb	<10	<20	<20	-
Si	<10	<1000	<1000	-
Sn	<10	-	-	-
Zn	-	-	-	6

Table 9 - Composition of Hoganas braze alloy. [51]

Comp. wt%	Ni	Cr	P	Si
BrazeLet Ni613	Bal.	29	6	4

Table 10 – Percent composition of 316L Stainless Steel. [52]

Element	316L
Cr	16—18
Ni	10—12
Mo	2—3
Si	< 1
P	< 1
S	< 1